Volume 50
Number 4
28 January 2021
Pages 1129-1516

Dalton Transactions

An international journal of inorganic chemistry

rsc.li/dalton

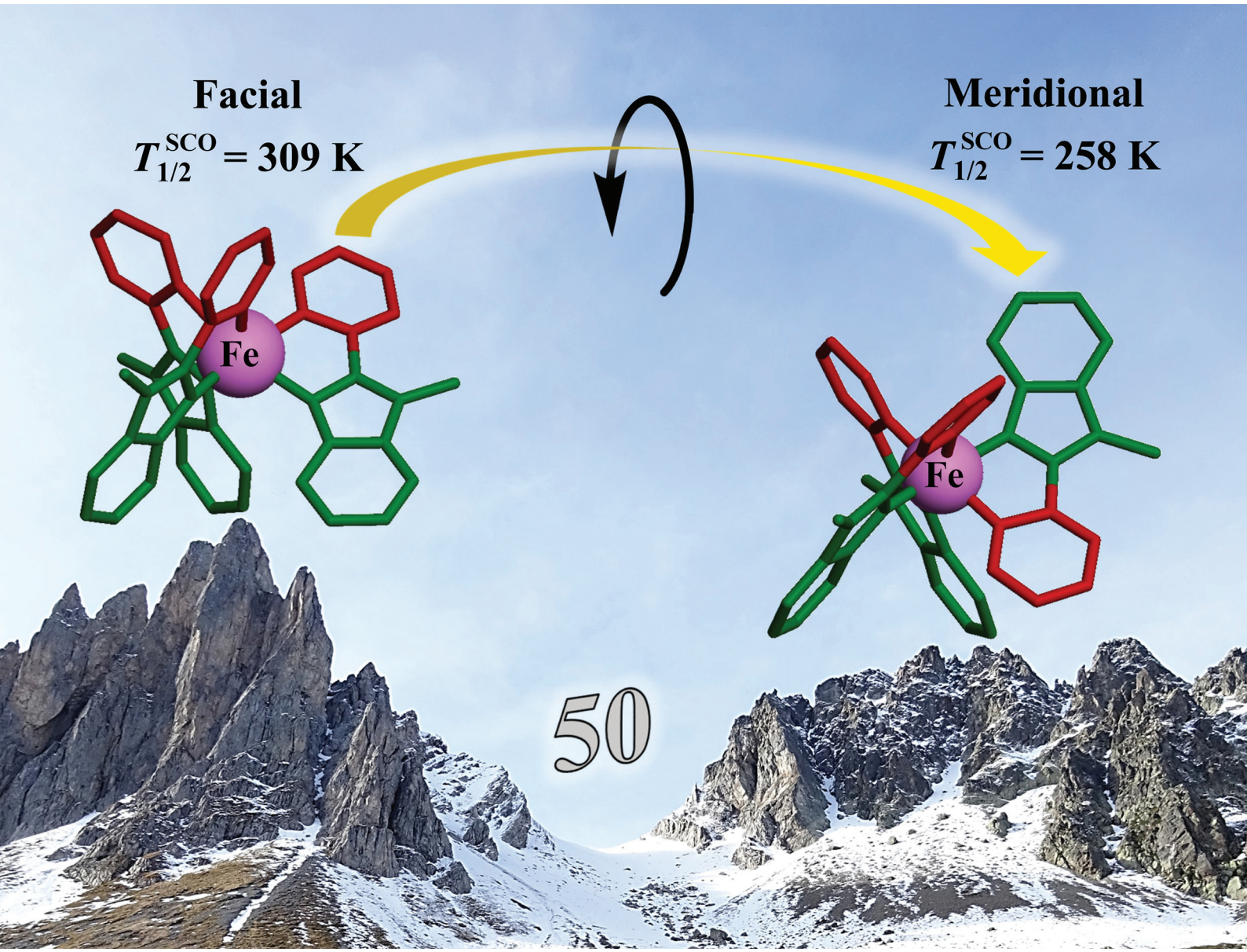

ISSN 1477-9226

ROYAL SOCIETY OF CHEMISTRY

PAPER

Claude Piguet *et al.*

Tuning spin-crossover transition temperatures in non-symmetrical homoleptic meridional/facial $[Fe(didentate)_3]^{2+}$ complexes: what for and who cares about it?

50 Anniversary Volume

Dalton Transactions

ROYAL SOCIETY OF CHEMISTRY

PAPER

View Article Online
View Journal | View Issue

Check for updates

Cite this: *Dalton Trans.*, 2021, **50**, 1206

Tuning spin-crossover transition temperatures in non-symmetrical homoleptic meridional/facial $[Fe(didentate)_3]^{2+}$ complexes: what for and who cares about it?†

Neel Deorukhkar,[a] Céline Besnard,[b] Laure Guénée[b] and Claude Piguet *[a]

The $[FeN_6]$ chromophores found in $[Fe(didentate)_3]^{2+}$ complexes, where didentate is a non-symmetrical 2-(6-membered-heterocyclic ring)-benzimidazole ligand (**L*k***), exist as mixtures of two geometrical *mer* (C_1-symmetry) and *fac* (C_3-symmetry) isomers. Specific alkyl-substituted six-membered heterocyclic rings connected to the benzimidazole unit (pyridines in ligands **L1–L3**, pyrazines in **L4–L5** and pyrimidines in **L6–L7**) control the ligand field strength and the electron delocalization so that $[Fe^{II}(\mathbf{Lk})_3]^{2+}$ display tunable thermally-induced spin transitions in solution. Thermodynamic, spectroscopic (UV-Vis, NMR) and magnetic studies in solution demonstrate that $[Fe(\mathbf{L6})_3]^{2+}$ (**L6** = 1-methyl-2-(pyrimidin-2-yl)-1*H*-benzo[*d*]imidazole) exhibits a close to room temperature spin transition ($T_{1/2}$ = 273(3) K) combined with a high stability formation constant ($\log(\beta_{1,3}^{Fe,\mathbf{L6}}) = 21.8(9)$ in acetonitrile), which makes this complex suitable for the potential modulation of lanthanide-based luminescence in polymetallic helicates. A novel method is proposed for assigning specific thermodynamic spin crossover parameters to *fac*-$[Fe(\mathbf{L6})_3]^{2+}$ and *mer*-$[Fe(\mathbf{L6})_3]^{2+}$ isomers in solution. The observed difference relies mainly on the entropic content $\Delta S_{SCO}^{mer} - \Delta S_{SCO}^{fac}$ = 11(1) J mol^{-1} K^{-1}, which favors the spin transition for the meridional isomer. Intermolecular interactions occurring in the crystalline state largely overcome minor thermodynamic trends operating in diluted solutions and a single configurational isomer is usually observed in the solid state. Among the thirteen solved crystal structures **1–13** containing the $[M(\mathbf{Lk})_3]^{2+}$ cations (M = Fe, Ni, Zn, **L*k*** = **L6–L7**), pure meridional isomers are observed six times, pure facial isomers also six times and a mixture (44% *mer* and 56% *fac*) is detected only once. Solid-state magnetic data recorded for the Fe^{II} complexes show the operation of slightly cooperative spin transitions in **7** (*fac*-$[Fe(\mathbf{L6})_3]^{2+}$) and **12** (*mer*-$[Fe(\mathbf{L7})_3]^{2+}$). For the meridional isomer in **6**, a two-step spin state transition curve, associated with two phase transitions, is detected.

Received 6th November 2020,
Accepted 15th December 2020

DOI: 10.1039/d0dt03828h

rsc.li/dalton

Introduction

Faced with the duality of paramagnetism measured for $[Fe(H_2O)_6]^{2+}$ and diamagnetism for $[Fe(CN)_6]^{4-}$, Pauling exploited valence bond theory in 1931 to develop the concept of 'magnetic criterion of bond type' (Scheme 1a).[1,2] He also recognized that two molecular systems with different spin states could be present simultaneously at a given temperature, according that the energy difference between them is comparable with thermal energy (mRT with $1 \leq m \leq 10$).[3,4] The concomitant isolation by Cambi *et al.* of Fe^{III} complexes with dithiocarbamate ligands displaying thermal spin-state equilibria are still considered as the first experimental demonstration of what is known as the spin crossover (SCO) phenomenon.[5–7] The formulation of the crystal-field theory,[8] further extended and improved by the ligand field theory,[9–11] provided a better description of chemical bonding for open-shell transition metal complexes (Scheme 1b). The SCO phenomenon exhibited by d^6 Fe^{II} in an octahedral environment could be then quantified as twice the difference between the ligand field strength Δ_{oct} and the spin pairing energy P, the latter being modeled with the help of the Racah parameters B and C to give $P = 2B + 4C \approx 19B$ (Scheme 1b).[12] A complete ligand-field picture is provided by the relevant Tanabe–Sugano diagram, which displays the relative energies of all the Russell–Saunders multiplet terms arising from the d^6 configuration as a function of the Δ_{oct}/B ratio (Scheme 1c).[13]

The strict equality $\Delta_{oct} = P$, $E_{HS}^{\circ} - E_{LS}^{\circ} = 2(\Delta_{oct} - P) = 0$, leads to $\Delta_{oct}/B \approx 19$ and an equal population of $^1A_1$ and $^5T_2$

[a]*Department of Inorganic and Analytical Chemistry, University of Geneva, 30 quai E. Ansermet, CH-1211 Geneva 4, Switzerland. E-mail: Claude.Piguet@unige.ch*
[b]*Laboratory of Crystallography, University of Geneva, 24 quai E. Ansermet, CH-1211 Geneva 4, Switzerland*

† Electronic supplementary information (ESI) available. CCDC 2041614–2041630. For ESI and crystallographic data in CIF or other electronic format see DOI: 10.1039/d0dt03828h

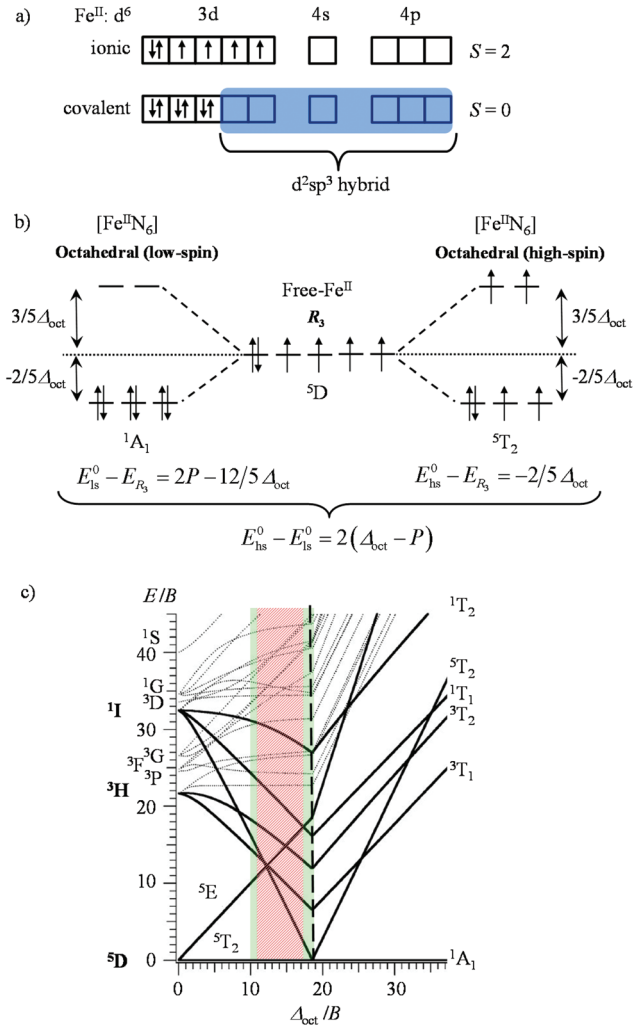

Scheme 1 a) Illustration of early Pauling's magnetic criterion of bond type; (b) crystal field/ligand field approach to spin crossover phenomenon (*P* is the electron spin pairing energy); (c) Tanabe–Sugano diagram for a d^6 metal ion completed with a central red domain, which corresponds to non-accessible ligand-field strengths and green domains where low-spin and high-spin complexes co-exist at accessible temperatures ($0 \leq \{E^\circ_{hs} - E^\circ_{ls}\} \leq 2000\ cm^{-1}$). Adapted from ref. 16 and 17.

levels represented by a vertical dashed line (Scheme 1c). However, this approach is misleading and physically unsound since the vertical dashed line in the Tanabe–Sugano diagram (Scheme 1c) refers to a non-equilibrium geometry. Indeed, the population of the antibonding orbitals in high-spin Fe^{II} is accompanied by a 10% elongation of the Fe–N bond lengths[14] together with minor geometrical distortions,[15] which affect Δ_{oct} and *P* during the spin transition. Taking this into account, a domain in the Tanabe–Sugano diagram is no more accessible to coordination complexes (red surface in Scheme 1c), whereas two restricted domains (green surfaces in Scheme 1c) correspond to the limits $11\,000 \leq \Delta^{HS}_{oct} \leq 12\,500\ cm^{-1}$ and $19\,000 \leq \Delta^{LS}_{oct} \leq 22\,000\ cm^{-1}$ for which the phenomenon of a thermal spin transition ($\Delta E = E^\circ_{HS} - E^\circ_{LS} = mRT$ with $1 \leq m \leq 10$) can be expected in Fe^{II} coordination complexes with standard Racah parameters.[12,16] Consequently, an adequate modeling of SCO behaviors requires looking beyond ligand-field theory with the help of quantum chemistry for mapping quantitatively the energy surfaces at equilibrium geometries associated with the $^1A_1$ and $^5T_2$ terms.[21] Although significant progress is being made along this line,[18–23] reliable models for the prediction of molecular SCO systems are still limited because they involve open-shell species and small energy differences.[24] The systematic exploration of classes of ligands is thus the rule for designing molecular SCO complexes in coordination chemistry. Myriads of six-coordinate SCO Fe^{II} complexes have been thus actively synthesized, characterized and *a posteriori* rationalized. This global effort has been regularly and extensively reviewed during the last two decades in specialized journals[14,25–35] and in two comprehensive monographies.[36,37] There is no doubt that the pseudo-octahedral [FeN$_6$] chromophore, where N stands for a heterocyclic nitrogen donor atom, is one of the most studied and versatile unit for implementing Fe^{II} SCO properties in molecular complexes. Some 'rules of thumb' could be extracted from empirical analyses of structure–properties relationships. For instance, Shatruk and coworkers used the interatomic separation between the N-donor atoms in multidentate chelate ligands as a metric guide for programming SCO properties in Fe^{II} complexes,[38] whereas Brooker, Garden and coworkers reported on more sophisticated density functional theory (DFT) calculations for predicting the ^{15}N NMR shifts in 1,2,4-triazole ligands, which can be then used as a criterion for rationalizing SCO behaviors.[24]

Short-range and long-range orders produced by packing interactions in solid state samples drastically complicate the situation because intermolecular energies usually dominate the minor energy changes accompanying the spin state transition at the molecular level,[30,39–42] a phenomenon often at the origin of specific phase transitions accompanying the spin crossover process in the solid state.[39,43] Whereas spin-state transitions implying solvated complexes in solution can be satisfyingly modeled with the standard entropy of mixing according to the simple chemical equilibrium (1) and associated stability constant K_{SCO},[44,45] intermolecular communications produce some cooperative effects in the solid state, which can be implemented either by adding an interaction term $\Gamma(x_{hs}, T, P) = \gamma \cdot x_{hs} \cdot (1 - x_{hs})$ to give eqn (2), where γ is an adjustable interaction parameter,[43,46] or by considering non-randomly distributed domains containing *n* molecules of like spin in eqn (3) and (4), where C_p are the heat capacities at constant pressure.[43,47]

$$Fe^{II}_{low\text{-}spin} \overset{K_{SCO}}{\rightleftharpoons} Fe^{II}_{high\text{-}spin}$$
$$-\ln(K_{SCO}) = \ln\left(\frac{1 - x_{hs}}{x_{hs}}\right) = \frac{\Delta G_{SCO}}{RT} = \frac{\Delta H_{SCO}}{RT} - \frac{\Delta S_{SCO}}{R} \quad (1)$$

$$\ln\left(\frac{1 - x_{hs}}{x_{hs}}\right) = \frac{\Delta H_{SCO} + \gamma(1 - 2x_{hs})}{RT} - \frac{\Delta S_{SCO}}{R} \quad (2)$$

$$\ln\left(\frac{1-x_{hs}}{x_{hs}}\right) = \frac{n\Delta G_{SCO}}{RT} = \frac{n\Delta H_{SCO}}{RT} - \frac{n\Delta S_{SCO}}{R} \quad (3)$$

with

$$n = \frac{4RT_{1/2}}{\Delta H^2_{SCO}}\left[C_p(T_{1/2}) - \frac{C_{p\text{-}LS}(T_{1/2}) + C_{p\text{-}HS}(T_{1/2})}{2}\right] \quad (4)$$

Since precise chemical programming of spin state transitions are not accessible in solution, there is much less chance to propose some reliable design in solids, and major interest in the SCO community moved toward the systematic structural exploration of classes of ligands and complexes for designing addressable (*via* temperature, pressure, light) switches implemented in various materials (solids, films, nanoparticles, liquid crystals, *etc.*).[37,48–53] The deliberate combination of SCO properties with other physical or chemical properties in a synergetic fashion in molecular entities, summarized under the term of multifunctionality,[54–56] remains in its infancy despite remarkable efforts focused on the modulation of magnetic communication[57,58] and luminescence.[59] For instance, the modulation of an emissive lanthanide by an adjacent SCO Fe^{II} metallic site in an isolated dimetallic complex has been recently attempted (Fig. 1), but it proved to depend crucially on some ultra-precise tuning of the spin state equilibrium, which is currently beyond rational chemical design.[60]

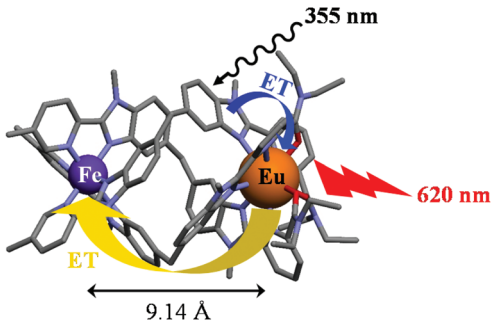

Fig. 1 Molecular structure of the $[EuFeL_3]^{5+}$ helicate in which red luminescence (620 nm) is modulated *via* energy transfer (ET) to the adjacent SCO Fe^{II} unit.[60]

Starting from the didentate 2-(α-methyl-substituted pyridine)-benzimidazole ligands **L1–L3** (Scheme 2), which exactly model the didentate units bound to Fe^{II} in the $[EuFeL_3]^{5+}$ helicate, some systematic exploration of structurally related 2-(α-methyl-substituted pyrazine)-benzimidazole **L4–L5** allowed some shifts of $T_{1/2}$ in the mononuclear $[Fe(didentate)_3]^{2+}$ model complexes, but none of them improved the situation in

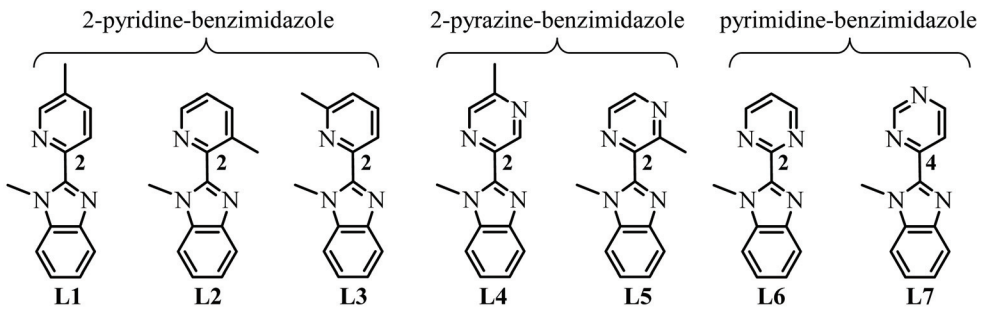

Complex	$[Ni(\mathbf{L1})_3]^{2+}$	$[Ni(\mathbf{L2})_3]^{2+}$	$[Ni(\mathbf{L3})_3]^{2+}$	$[Ni(\mathbf{L4})_3]^{2+}$	$[Ni(\mathbf{L5})_3]^{2+}$	$[Ni(\mathbf{L6})_3]^{2+}$	$[Ni(\mathbf{L7})_3]^{2+}$
Δ_{oct} /cm^{-1}	11423	10681	9644	11476	11555	11605	11385
B /cm^{-1}	889	918	994	866	866	865	870
Δ_{oct}/B	12.9	11.6	9.7	13.3	13.3	13.4	13.1
Complex	$[Fe(\mathbf{L1})_3]^{2+}$	$[Fe(\mathbf{L2})_3]^{2+}$	$[Fe(\mathbf{L3})_3]^{2+}$	$[Fe(\mathbf{L4})_3]^{2+}$	$[Fe(\mathbf{L5})_3]^{2+}$	$[Fe(\mathbf{L6})_3]^{2+}$	$[Fe(\mathbf{L7})_3]^{2+}$
ΔH_{SCO} / kJ·mol^{-1}	28.3(4)	High-Spin	High-Spin	35.0(3)	High-Spin	19.5(2)	23.0(2)
ΔS_{SCO} / J·mol^{-1}·K^{-1}	91(1)	High-Spin	High-Spin	100(1)	High-Spin	71.3(6)	82.5(8)
$T_{1/2}$ /K	309(6)	High-Spin	High-Spin	349(5)	High-Spin	273(3)	279(1)
Reference	61	61	61	61	16	This work	This work

Scheme 2 Chemical structures of the didentate ligands **L1–L7**, together with the electronic properties of the associated pseudo-octahedral $[Ni(\mathbf{Lk})_3]^{2+}$ complexes and thermodynamic SCO properties of the pseudo-octahedral $[Fe(\mathbf{Lk})_3]^{2+}$ complexes in CD_3CN solutions.

the helicates.[16,61] Moreover, simple mononuclear $[Fe(didentate)_3]^{2+}$ complexes exist as mixtures of meridional and facial isomers, for which only the latter one can be taken as a valuable model for the triple-stranded $[EuFe\mathbf{L}_3]^{5+}$ helicates.[61]

We report here the connection of a 2-pyrimidine ring (**L6**) or a 4-pyrimidine ring (**L7**) to the benzimidazole ring, which eventually provides $[Fe(\mathbf{Lk})_3]^{2+}$ complexes possessing lower transition temperatures compatible with luminescence modulation in triple-stranded helicates (Scheme 2). A novel approach for the estimation of specific thermodynamic SCO parameters for meridional and facial isomers in solution is described.

Results and discussion

Design, synthesis and characterization of the didentate pyrimidine–benzimidazole ligands L6 and L7

In an elegant contribution,[24] Brooker, Garden and co-workers suggested that the ^{15}N NMR chemical shifts recorded for the binding nitrogen atom of the azine ring in a series of didentate triazole–azine ligands ($\mathbf{L}^{Azine}$) can be taken as a valuable indicator for both the electronic density borne by the N-donor atoms and their capacity to control the critical temperature $T_{1/2}$ of spin transitions for $[Fe(\mathbf{L}^{Azine})_2(NCBH_3)_2]$ in solution. The decreasing order found for $T_{1/2}$ (pyrazine > pyridine > pyrimidine) matches that reported in Scheme 2 for the two first related complexes $[Fe(\mathbf{L4})_3]^{2+}$ (pyrazine) > $[Fe(\mathbf{L1})_3]^{2+}$ (pyridine) and encourages us to prepare 2-pyrimidine (**L6**) and 4-pyrimidine (**L7**) analogues for (i) shifting $T_{1/2}$ toward lower temperatures in $[Fe(\mathbf{Lk})_3]^{2+}$ and (ii) further exploring the effect of meridional ↔ facial isomerization on the SCO properties.

The ligands **L6–L7** were thus synthesized (Scheme 3) using a well-established strategy based on modified Philips condensation reactions for the formation of benzimidazoles as key steps.[62] Pyrimidine-carboxylic acids, contrary to pyrazine-2-carboxylic acid,[16,62] could be activated *in situ* to pyrimidine-2-carbonyl chloride through standard reactions with either thionyl chloride or oxalyl chloride. The ^1H NMR and ^{13}C NMR spectra (Scheme 4a and Fig. S1–S12†) point to fast rotations around the inter-annular C–C bond leading to average C_s-symmetry on the NMR time scale. The lack of NOE effect between the protons of the methyl group of the benzimidazole and the pyrimidine proton at the 5-position of the pyrimidine in **L7** suggests a preferred average planar conformation in solution with an *anti* location of the N-donor atoms in the free didentate ligand (shown in Schemes 3 and 4). These structural characteristics are supported by gas-phase energies computed as a function of the interplanar angle between the two aromatic rings (Fig. S13†). Finally, indirect ^1H–^{15}N detection (Fig. S6 and S12†)[63] shows that the N-donor atom of 2-pyrimidine in **L6** is less shielded than that in 4-pyridimidine in **L7** (Scheme 4b), an experimental result which is confirmed by the larger negative charge computed for the azine donor group in **L7** (Fig. S14†).

Slow diffusion of *n*-hexane into concentrate solutions of **L6** and **L7** in dichloromethane yielded crystals suitable for X-ray diffraction analysis (Tables S1–S6 and Fig. S15–S20†). Each unit cell contains two slightly different molecules of the ligands, both confirming the formation of almost planar didentate aromatic units adopting *anti* arrangements of the N-donor atoms (Fig. 2).

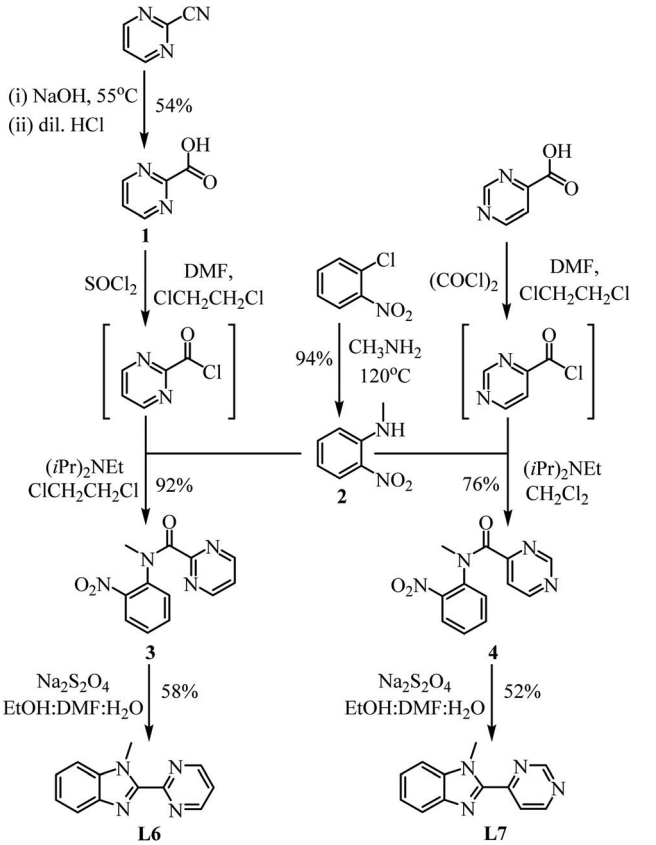

Scheme 3 Multistep synthesis of the didentate ligands **L6** (2-pyrimidine) and **L7** (4-pyrimidine).

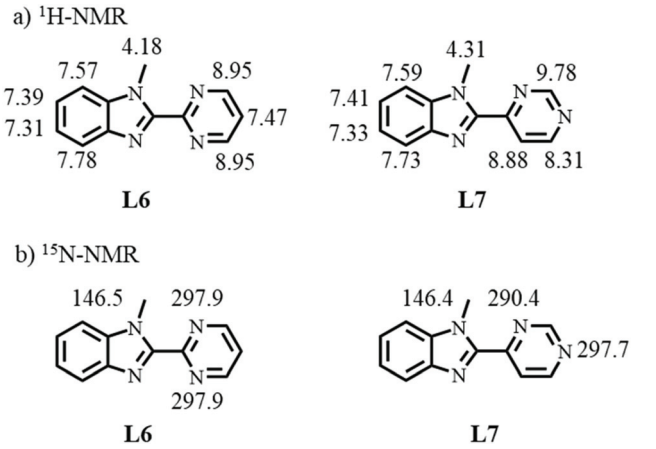

Scheme 4 a) ^1H NMR chemical shifts (with respect to tetramethylsilane at 0 ppm in CD_3CN) and (b) ^{15}N NMR chemical shifts (with respect to nitromethane at 381.7 ppm in CD_2Cl_2) observed for ligands **L6** and **L7**.

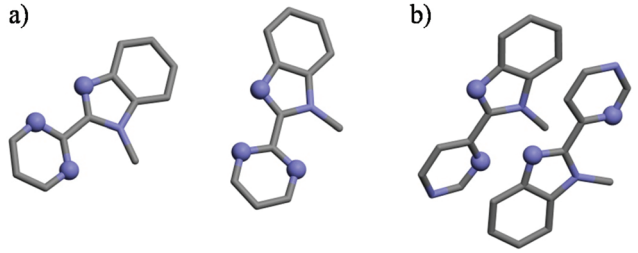

Fig. 2 Molecular structures of the two different molecules in the unit cells of the crystal structures of (a) **L6** (interplanar angles 5.93(5)° and 9.71(5)°) and (b) **L7** (interplanar angles 7.65(8)° and 12.73(8)°). The N-donor atoms are highlighted as blue spheres.

Complexation of the didentate pyrimidine–benzimidazole ligands L6 and L7 with Zn^{II}, Ni^{II} and Fe^{II} in solution

Reactions of **L6** or **L7** with $M(CF_3SO_3)_2$ (M = Zn, Fe) or $Ni(BF_4)_2$ in acetonitrile is characterized by a red-shift of the ligand-centered $\pi^* \leftarrow n,\pi$ electronic transitions (Fig. S21a–S24a†). Similar shifts were originally reported for 2,2′-bipyridine,[64] and could be theoretically assigned to the *anti* → *syn* conformational change of the α,α′-diimine binding unit accompanying its chelate complexation to the metal.[65,66] The spectrophotometric titrations of submillimolar concentrations of the ligands **L6** and **L7** in dry acetonitrile with $Zn(CF_3SO_3)_2$ were therefore exploited for the quantitative analysis of the successive formation of three complexes, characterized by smooth endpoints at Zn/**L*k*** = 1 : 3, Zn/**L*k*** = 1 : 2, Zn/**L*k*** = 1 : 1 (Fig. S21b–S22b†). This trend was further confirmed by factor analysis (Fig. S21c–S22c†), which suggested the existence of four individual absorbing eigenvectors **L*k***, Zn**L*k***, $Zn(\mathbf{L}k)_2$ and $Zn(\mathbf{L}k)_3$ with satisfying re-constructed absorption spectra (Fig. S21d–S22d†).[67–70] Non-linear least-squares fit to equilibria (5)–(7) provided satisfying estimates for the formation macroconstants $\beta_{1,n}^{M,\mathbf{L}k}$ gathered in Table 1 (column 1, entries 1 and 2).[71–73]

$$M^{2+} + \mathbf{L}k \rightleftharpoons [M(\mathbf{L}k)]^{2+}\beta_{1,1}^{M,\mathbf{L}k} \quad (5)$$

$$M^{2+} + 2\mathbf{L}k \rightleftharpoons [M(\mathbf{L}k)_2]^{2+}\beta_{1,2}^{M,\mathbf{L}k} \quad (6)$$

$$M^{2+} + 3\mathbf{L}k \rightleftharpoons [M(\mathbf{L}k)_3]^{2+}\beta_{1,3}^{M,\mathbf{L}k} \quad (7)$$

Taking the experimental ^{15}N HMR chemical shifts (Scheme 4b) as a body of evidence for optimizing *M*-σL binding and stability upon coordination to spherical and ionic Zn^{2+}, one can reasonably predict $\beta_{1,n}^{Zn,L7} > \beta_{1,n}^{Zn,L6}$. However, the reverse situation holds with a cumulative constant $\log(\beta_{1,3}^{Zn,L7}) = 14.07(4)$, found for $[Zn(\mathbf{L7})_3]^{2+}$, being almost 8 orders of magnitude smaller than $\log(\beta_{1,3}^{Zn,L6}) = 21.8(1)$ (Table 1). Translated into ligand speciation,[73] these thermodynamic constants imply that the target saturated complex $[Zn(\mathbf{L6})_3]^{2+}$ is quantitatively formed (>98%) in solution for a stoichiometric ratio Zn : **L6** = 1 : 3 and a total ligand concentration of 10 mM (Fig. 3a). For $[Zn(\mathbf{L7})_3]^{2+}$, a maximum of 82% of this complex can be detected in acetonitrile for a total ligand concentration of 10 mM (Fig. 3b). Its quantitative formation (≥97%) requires a ten times larger total concentration of ligand **L7** (100 mM, Fig. 3c).

We conclude that σ-donation from the bound ligand to Zn^{2+} is not the only important thermodynamic driving force. Comparison with the previous azine found in $[Zn(\mathbf{L4})_n]^{2+}$ (Table S7†)[74] shows that **L4** (2-pyrazine, $pK_a = 0.65$), which is a much weaker σ-donor but a stronger π-acceptor than **L7**, indeed provides stability constants up to three orders of magnitude larger than those observed for $[Zn(\mathbf{L7})_n]^{2+}$ (4-pyrimidine, $pK_a = 1.23$). Surprisingly, the stability constants of $[Zn(\mathbf{L6})_n]^{2+}$ (2-pyrimidine, $pK_a = 1.23$) largely overcome those of its azine analogues with **L4** and **L7**, and can be only compared with that produced by the more basic 2-pyridine ring (pK_a = 5.2) in $[Zn(\mathbf{L1})_n]^{2+}$ (Table S7†). In fact, the complexation of **L1**, **L4** and **L7** with the entering cation is limited by some considerable energetic penalties accompanying the *anti* → *syn* conformational change of the chelate α,α′-diimine unit. On the contrary, **L6** is 'symmetrically preorganized' and no ligand reorganization is required. This beneficial effect is reminiscent to the gain of four orders of magnitude in stability observed in going from $[Zn(2,2'\text{-bipyridine})_3]^{2+}$ ($\log(\beta_{1,3}) = 13.2(2)$) to $[Zn(1,10\text{-phenanthroline})_3]^{2+}$ ($\log(\beta_{1,3}) = 17.1(1)$) in water.[75]

Table 1 Stability constants for the successive formation of $[M(\mathbf{L}k)_n]^{2+}$ (M = Zn, Ni, Fe, **L*k*** = **L6**, **L7**, *n* = 1, 2, 3, non-coordinating anions: ClO_4^-, $CF_3SO_3^-$ or BF_4^-) in acetonitrile (293 K), metal–ligand interaction parameter ($f^{M,\mathbf{L}k}$) and inter-ligand interaction parameter ($u^{\mathbf{L}k,\mathbf{L}k}$), and associated energies $\Delta G_{affinity} = -RT\ln(f^{M,\mathbf{L}k})$ and $\Delta E_{interaction} = -RT\ln(u^{\mathbf{L}k,\mathbf{L}k})$

		$\log(f^{M,L})$	$\Delta G_{affinity}$/kJ mol^{-1}	$\log(u^{L,L})$	$\Delta E_{interaction}$/kJ mol^{-1}
$[Zn(L6)_n]^{2+}$	$\log(\beta_{1,1}) = 7.02(4)$ $\log(\beta_{1,2}) = 15.2(1)$ $\log(\beta_{1,3}) = 21.8(1)$	6.0(4)	−34.4(2.4)	0.7(5)	−3.6(2.8)
$[Zn(L7)_n]^{2+}$	$\log(\beta_{1,1}) = 5.10(1)$ $\log(\beta_{1,2}) = 10.22(2)$ $\log(\beta_{1,3}) = 14.07(4)$	3.9(2)	−22.1(9)	0.2(2)	−1.3(1.1)
$[Fe(L6)_n]^{2+}$	$\log(\beta_{1,1}) = 5.0(1)$ $\log(\beta_{1,2}) = 10.95(1)$ $\log(\beta_{1,3}) = 15.70(1)$	4.1(5)	−23.2(2.7)	0.3(6)	−1.6(3.2)
$[Ni(L7)_n]^{2+}$	$\log(\beta_{1,1}) = 4.11(1)$ $\log(\beta_{1,2}) = 9.22(1)$ $\log(\beta_{1,3}) = 13.65(1)$	3.0(2)	−16.8(1.3)	1.0(3)	−5.8(1.5)

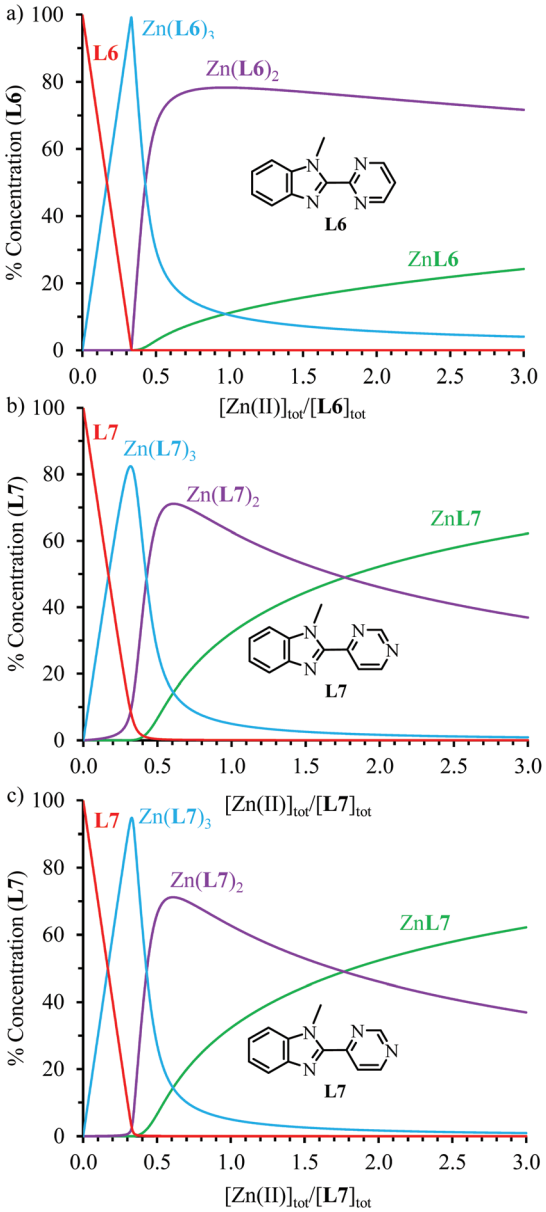

Fig. 3 Concentration profiles obtained using HySS2009 simulation[73] and the formation constants collected in Table 1 for the complex species (a) $[Zn(\mathbf{L6})_n]^{2+}$ at $|\mathbf{L6}|_{tot}$ = 10 mM, and (b and c) $[Zn(\mathbf{L7})_n]^{2+}$ at (b) $|\mathbf{L7}|_{tot}$ = 10 mM and (c) $|\mathbf{L7}|_{tot}$ = 100 mM (acetonitrile, 293 K).

A deeper and quantitative analysis relies on the site binding model (eqn (8)),[76–78] which combines a statistical factor $K_{1,n}^{stat}$ (related to the contribution produced by the change in rotational entropy between the reactants and products and to the entropy of mixing of enantiomers),[79–81] with a chemical contribution $K_{1,n}^{chem}$ made up of two microscopic chemical parameters $f_i^{M,\mathbf{Lk}}$ and $u_{k,l}^{\mathbf{Lk},\mathbf{Lk}}$. The first term $f_i^{M,\mathbf{Lk}} = e^{-\left(\Delta G_{1,i,affinity}^{M,\mathbf{Lk}}/RT\right)}$ stands for the intermolecular microscopic affinities (including desolvation) characterizing the free energy of inner sphere connection of the didentate binding site in **Lk** to M^{II} $\left(\Delta G_{i,affinity}^{M,\mathbf{Lk}} = -RT\ln\left(f_i^{M,\mathbf{Lk}}\right)\right)$ and $u_{k,l}^{\mathbf{Lk},\mathbf{Lk}} = e^{-\left(\Delta E_{k,j}^{\mathbf{Lk},\mathbf{Lk}}/RT\right)}$ accounts for the free energy of interligand interactions $\left(\Delta E_{k,l}^{\mathbf{Lk},\mathbf{Lk}} = -RT\ln\left(u_{k,l}^{\mathbf{Lk},\mathbf{Lk}}\right)\right)$, which operate when two ligands are bound to the same metallic centre.

$$\beta_{1,n}^{M,\mathbf{Lk}} = e^{-\Delta G_{1,n}^{M,\mathbf{Lk}}/RT} = K_{1,n}^{stat}\cdot K_{1,n}^{chem} = K_{1,n}^{stat}\cdot\left(\prod_{i=1}^{n} f_i^{M,\mathbf{Lk}}\cdot\prod_{k<l} u_{k,l}^{\mathbf{Lk},\mathbf{Lk}}\right) \quad (8)$$

Application of eqn (8) to all possible geometric isomers of pseudo-octahedral $[Zn(\mathbf{Lk})(S)_4]^{2+}$ (one isomer, S = solvent), $[Zn(\mathbf{Lk})_2(S)_2]^{2+}$ (five stereoisomers) and $[Zn(\mathbf{Lk})_3]^{2+}$ (two stereoisomers) has been previously detailed (Fig. S25†)[74] and provides eight micro-constants which can be combined to give a global model (eqn (9)–(11)) for the three macro-constants characterizing equilibria (5)–(7).

$$\beta_{1,1}^{Zn,\mathbf{Lk}} = 24 f^{Zn,\mathbf{Lk}} \quad (9)$$

$$\beta_{1,2}^{Zn,\mathbf{Lk}} = 12\left(f^{Zn,\mathbf{Lk}}\right)^2\left(u_{trans,fac}^{\mathbf{Lk},\mathbf{Lk}} + u_{trans,mer}^{\mathbf{Lk},\mathbf{Lk}} + 4u_{cis,fac}^{\mathbf{Lk},\mathbf{Lk}} + 4u_{cis,mer}^{\mathbf{Lk},\mathbf{Lk}}\right) \quad (10)$$

$$\beta_{1,3}^{Zn,\mathbf{Lk}} = 16\left(f^{Zn,\mathbf{Lk}}\right)^3 u_{cis,fac}^{\mathbf{Lk},\mathbf{Lk}}\left[\left(u_{cis,fac}^{\mathbf{Lk},\mathbf{Lk}}\right)^2 + 3\left(u_{cis,mer}^{\mathbf{Lk},\mathbf{Lk}}\right)^2\right] \quad (11)$$

Assuming the operation of a single average intermetallic interaction $u_{trans,fac}^{\mathbf{Lk},\mathbf{Lk}} \simeq u_{trans,mer}^{\mathbf{Lk},\mathbf{Lk}} \simeq u_{cis,fac}^{\mathbf{Lk},\mathbf{Lk}} \simeq u_{cis,mer}^{\mathbf{Lk},\mathbf{Lk}} \equiv u_{\mathbf{Lk},\mathbf{Lk}}$ reduces the number microscopic descriptors to $f^{Zn,\mathbf{Lk}}$ and $u^{\mathbf{Lk},\mathbf{Lk}}$ for modelling the three macroscopic constants obtained by spectrophotometry (eqn (9), (12) and (13)).

$$\beta_{1,2}^{Zn,\mathbf{Lk}} = 120\left(f^{Zn,\mathbf{Lk}}\right)^2 u^{\mathbf{Lk},\mathbf{Lk}} \quad (12)$$

$$\beta_{1,3}^{Zn,\mathbf{Lk}} = 64\left(f^{Zn,\mathbf{Lk}}\right)^3\left(u^{\mathbf{Lk},\mathbf{Lk}}\right)^3 \quad (13)$$

Linear least-squares fits of the logarithmic forms provide the affinity parameters $\Delta G_{affinity}^{Zn,\mathbf{Lk}} = -RT\ln\left(f^{Zn,\mathbf{Lk}}\right)$ and interligand interactions $\Delta E_{interaction}^{\mathbf{Lk},\mathbf{Lk}} = -RT\ln\left(u^{\mathbf{Lk},\mathbf{Lk}}\right)$ gathered in Table 1 (columns 3–6), which satisfyingly reproduce the experimental data. Altogether, this rough thermodynamic model establishes that (i) the affinity of the selected didentate ligands for spherical Zn^{2+} $\left(-\Delta G_{1,i,affinity}^{M,\mathbf{Lk}}\right)$ follows the trend **L1** (2-pyridine) ≈ **L6** (2-pyrimidine) > **L4** (2-pyrazine) ≫ **L7** (4-pyrimidine) and (ii) the successive binding of ligands leading to $[Zn(\mathbf{Lk})_3]^{2+}$ follows a weakly cooperative procedure $\left(\Delta E_{interaction}^{\mathbf{Lk},\mathbf{Lk}} \leq 0\right)$.

Repeating the spectrophotometric titrations for submillimolar concentrations of the ligands **L6** and **L7** in dry acetonitrile with $Fe(CF_3SO_3)_2$ lead to smoother endpoints for **L6** (Fig. S23†) and to only poor drifts for **L7**. Satisfying factor analysis and non-linear least-squares fit using equilibria (5)–(7) could be obtained for **L6**. The associated macro-constants $\beta_{1,n}^{Fe,\mathbf{Lk}}$ are however drastically reduced by two to five orders of magnitude in going from Zn^{2+}/**L6** (Table 1, entry 1) to Fe^{2+}/**L6**

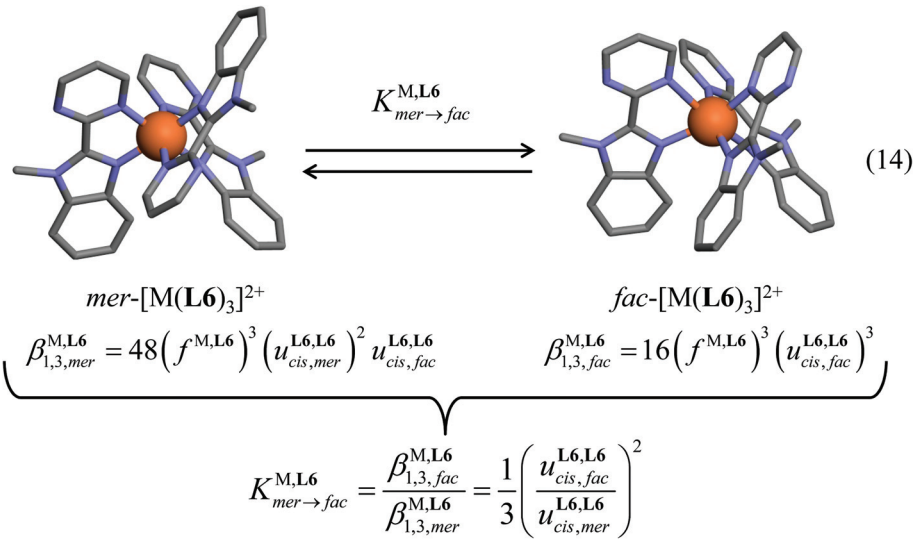

Fig. 4 Meridional to facial isomerization process operating in $[M(Lk)_3]^{2+}$ complexes (eqn (14)) together with its modeling with the help of the site binding model. The molecular structures are those found in the crystal structures of $[Zn(L6)_3](ClO_4)_2\,(CH_3CN)_{2.5}$ (**1**).

(Table 1, entry 3). Though less pronounced, the same trend was previously reported for 2-pyrazine-benzimidazole **L4** ligands in going from Zn^{2+} to Fe^{2+} (Table S7†).[61] The replacement of ligand **L6** with **L7** leads to $\beta^{Fe,L7}_{1,n} \ll \beta^{Fe,L6}_{1,n}$, a trend which strictly mirrors that previously observed for Zn^{2+}. Finally, titrations of **L7** with analogous Ni^{2+} cations (Fig. S24†) additionally fixes $\beta^{Fe,L7}_{1,n} \leq \beta^{Ni,L7}_{1,n}$ in line with the well-known Irving–Williams series (Table 1, entry 4).[16,82,83] Consequently, the speciation profiles computed for Fe^{2+}/**L6** (Fig. S26†) mirror those highlighted for Zn^{2+}/**L7** (Fig. 4b and c), which possess similar stability constants, but the Fe^{2+}/**L7** system is expected to produce much smaller quantities of $[Fe(L7)_3]^{2+}$, which are overcome by those computed for $[Ni(L7)_3]^{2+}$ (Fig. S27†).

Meridional to facial isomerization process operating for $[Zn(Lk)_3]^{2+}$ (**Lk** = **L6** and **L7**) in solution

A focus on the target $[M(Lk)_3]^{2+}$ complexes requires the variable-temperature analysis of the thermodynamic equilibrium (14) linking the meridional and facial isomers (Fig. 4). This challenge can be addressed for diamagnetic closed-shell $[Zn(Lk)_3]^{2+}$ cations with the help of variable-temperature ^{1}H NMR spectra.

At room temperature in CD_3CN and CD_3OD, both $[Zn(L6)_3]^{2+}$ (10 mM) and $[Zn(L7)_3]^{2+}$ (0.1 M) are quantitatively (>95%) formed and display dynamically average C_3-symmetrical symmetries on the NMR time scale (Fig. S28 and S29†). Upon stepwise decrease of the temperature, the dynamic exchange process slows down so that the ^{1}H NMR spectra display two series of resolved signals, which can be assigned to a mixture of *mer*-$[Zn(Lk)_3]^{2+}$ (C_1 symmetry, three signals for a given proton) and *fac*-$[Zn(Lk)_3]^{2+}$ (C_3 symmetry, one signal for a given proton, Fig. S28 and S29†). Integration of low temperature ^{1}H NMR data provides the experimental ratio of the concentrations *mer*-$[Zn(Lk)_3]^{2+}$/*fac*-$[Zn(Lk)_3]^{2+}$, from which $K^{Zn,Lk}_{mer\rightarrow fac}$ can be estimated at different temperatures. Van't Hoff plots display linear correlations (Fig. S30†) and lead to enthalpic and entropic contributions collected in Table 2 together with speciations highlighted in Fig. 5. As previously reported for *mer*-$[Zn(Lk)_3]^{2+}$ → *fac*-$[Zn(Lk)_3]^{2+}$ equilibria with **L1** (2-pyridine) and **L4** (2 pyrazine, Table S8†),[74] the latter *mer* → *fac* isomerization process for **L6** and **L7** is solvent dependent and deviates from a pure statistical behavior ($\Delta H^{Zn,Lk}_{mer\rightarrow fac} = 0$ and $-T\Delta S^{Zn,Lk}_{mer\rightarrow fac} = -RT\cdot\ln(1/3) = 2.7$ kJ mol^{-1} at 298 K).

The enthalpic preference for the facial isomer ($-7.3 \leq \Delta H^{Zn,Lk}_{mer\rightarrow fac} \leq -2.8$ kJ mol^{-1}, Table 2), in which each benzimidazole N-donor atom is bound trans to the N-atom of the pyridimidine ring, is reminiscent of the thermodynamic *trans* influence.[74,84] The opposite entropic preference for the meri-

Table 2 Thermodynamic enthalpic ($\Delta H^{Zn,Lk}_{mer\rightarrow fac}$) and entropic ($\Delta S^{Zn,Lk}_{mer\rightarrow fac}$) contributions to equilibrium (14) in solution

Complex	Solvent	ε_r [a]	$\Delta H^{Zn,Lk}_{mer\rightarrow fac}$/kJ mol^{-1}	$\Delta S^{Zn,Lk}_{mer\rightarrow fac}$/J mol^{-1} K^{-1}	$\Delta G^{Zn,Lk,\circ}_{mer\rightarrow fac}$ [b]/kJ mol^{-1}	$T_{1/2}$/K
$[Zn(L6)_3]^{2+}$	CD_3CN	37.5	−2.8(1)	−16.2(4)	2.1(2)	171(8)
$[Zn(L6)_3]^{2+}$	CD_3OD	33.0	−6.9(5)	−30(2)	2.2(5)	227(26)
$[Zn(L7)_3]^{2+}$	CD_3OD	33.0	−7.3(9)	−38(4)	3.8(1.5)	195(32)

[a] Relative dielectric constants. [b] $\Delta G^{Zn,Lk,\circ}_{mer\rightarrow fac}$ are calculated at T = 298 K.

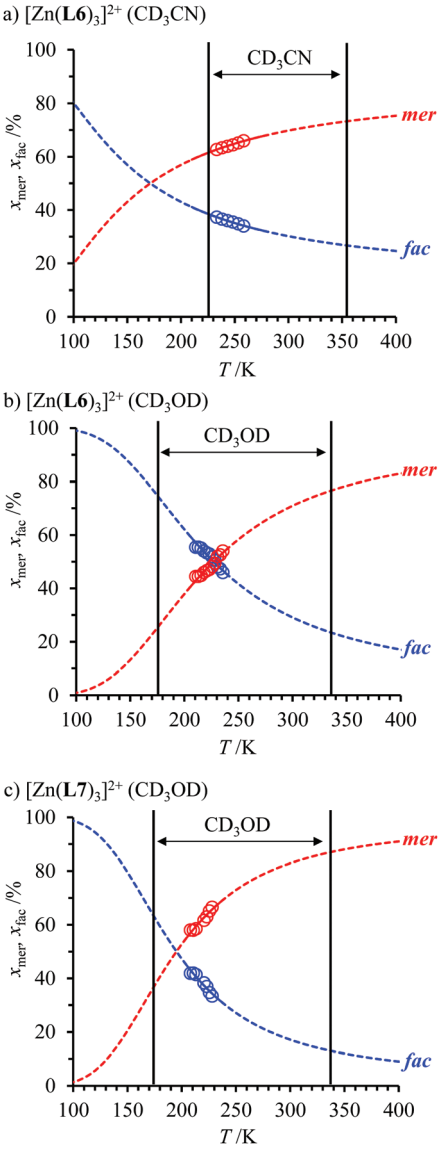

Fig. 5 Reconstruction of the mole fractions of the meridional and facial isomers for the complex $[Zn(\mathbf{L6})_3]^{2+}$ in (a) CD_3CN and (b) CD_3OD, and (c) for the complex $[Zn(\mathbf{L7})_3]^{2+}$ in CD_3OD as a function of temperature. The circles represent the accessible experimental data for which the dynamic of *mer* ↔ *fac* isomerization is slow on the ^1H NMR time scale.

dional isomer ($4.8 \leq -T\Delta S^{Zn,\mathbf{Lk}}_{mer\rightarrow fac} \leq 11.3$ kJ mol^{-1} at 298 K, Table 2), which is significantly larger than the pure statistical contribution of 2.7 kJ mol^{-1} at 298 K, has been previously attributed to the larger relaxation of the solvent organization around the meridional isomer which possesses a smaller dipole moment.[74]

Due to the remarkable stability found for $[Zn(\mathbf{L6})_3]^{2+}$ in solution, the kinetic rate constant of the *mer* ↔ *fac* isomerization process (eqn (14)) is small enough to give resolved ^1H NMR spectra for each isomer on the NMR time scale in acetonitrile prior to reach its freezing point ($233 \leq T \leq 258$ K, Fig. 6a and S28†). The situation changes with the less stable $[Zn(\mathbf{L7})_3]^{2+}$ complex, and the coalescence temperature for the

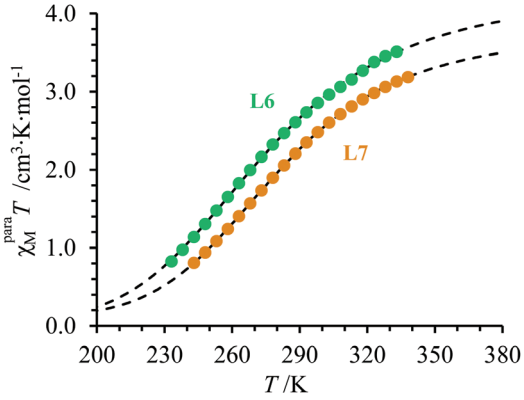

Fig. 6 Plot of molar paramagnetic magnetic susceptibility ($\chi_M^{para}T$) *versus* temperature (T) for a 10.2 mM solution of the complex $[Fe(\mathbf{L6})_3]^{2+}$ in CD_3CN (green), and a 21.3 mM solution of the complex $[Fe(\mathbf{L7})_3]^{2+}$ in CD_3CN (orange). The black dashed curves represent the best fit obtained by using eqn (20) and the thermodynamic and magnetic parameters collected in Table 3.

^1H NMR signals lie below the freezing point of CD_3CN (228 K). In deuterated methanol, some resolved ^1H NMR signals can be obtained for $T < 228$ K (Fig. S29†) for both $[Zn(\mathbf{L6})_3]^{2+}$ (Fig. 5b) and $[Zn(\mathbf{L7})_3]^{2+}$ (Fig. 5c).

Electronic and spin crossover properties of $[Fe(\mathbf{L6})_3]^{2+}$ and $[Fe(\mathbf{L7})_3]^{2+}$ in solution

According to Busch and co-workers,[85] the easily accessible ligand field strengths measured for the pseudo-octahedral $[Ni(\mathbf{Lk})_3]^{2+}$ complexes can be used as a reliable benchmark ($11\,200 \leq \Delta_{oct}(Ni^{II}) \leq 12\,400$ cm^{-1}) for predicting and rationalizing spin-crossover operative in the related Fe^{II} complexes. The absorption spectra recorded for 0.1 M acetonitrile solution of $[Ni(\mathbf{Lk})_3]^{2+}$ ($\mathbf{Lk}$ = **L6**, **L7**, Fig. S31 and S32†) display $Ni(^3T_2 \leftarrow {}^3A_2)$ transitions at 11 079 cm^{-1} for **L6** and 11 237 cm^{-1} for **L7**, which can be used as estimates for Δ_{oct} (Table S9†).[61,86–88] Altogether, the four $[Ni(\mathbf{Lk})_3]^{2+}$ complexes ($\mathbf{Lk}$ = **L1**, **L4**, **L6** and **L7**) possess very similar electronic properties with an average value of $\Delta_{oct}/B = 13.2(2)$ compatible with SCO behavior around room temperature for the related $[Fe(\mathbf{Lk})_3]^{2+}$ complexes (Scheme 2).[61,85] Variable temperature ^1H NMR spectra recorded for 0.1 mM solution of $[Fe(\mathbf{L6})_3]^{2+}$ in acetonitrile (233–298 K) indeed unambiguously demonstrate the existence of temperature-dependent paramagnetic shifts which are diagnostic for the formation of increasing amounts of fast-relaxing high-spin Fe^{II} ($S = 2$) at high temperature (Fig. S33†). However, the broadening of the signals due to the combination of low-spin to high-spin transformation with thermally-activated *mer* ↔ *fac* isomerization prevents the change in chemical shifts to be exploited for extracting reliable speciation in solution and associated spin state equilibria.[89,90]

Alternatively, the total magnetic susceptibility of a paramagnetic solute χ_M^{para} (cm^3 mol^{-1}) can be obtained with the help of Evans' method,[45,91–93] adapted for the temperature dependence of solvent density[94] and for an adequate treatment of

the various diamagnetic corrections (eqn (15); $S_f = 4\pi/3$ is the shape factor of the superconducting magnet, ν_0 is the Larmor frequency of the spectrometer in Hz, $\Delta\nu = \nu_{ref} - \nu_{int}$ is the difference in Hz between the frequency of the standard (*tert*-butanol) in contact with the complex of interest ($\nu_{ref} = \delta_{ref}\cdot\nu_o$) and that of the standard ($\nu_{int} = \delta_{int}\cdot\nu_o$) placed in the coaxial tube in absence of complex, M is the molecular weight in g·mol^{-1} of the paramagnetic complex or of its diamagnetic analogue when Fe^{II} is replaced with Zn^{II}, and m is the concentration of the pertinent complex in g cm^{-3}, Fig. S34†).[95,96]

$$\chi_M^{para} = \frac{1}{\nu_o S_f}\left(\frac{\Delta\nu^{para}M^{para}}{m^{para}} - \frac{\Delta\nu^{dia}M^{dia}}{m^{dia}}\right) \quad (15)$$

Application of eqn (15) for the variable-temperature shifts of the ^{1}H-NMR signals recorded for *tert*-butanol in acetonitrile solutions of $[Fe(\mathbf{L6})_3]^{2+}$ (10.2 mM, Fig. S34†) and $[Fe(\mathbf{L7})_3]^{2+}$ (21.3 mM), while using $[Zn(\mathbf{L6})_3]^{2+}$ (13 mM) as the diamagnetic reference, eventually gave plots of $\chi_M^{para}T$ *versus* T, which are diagnostic for the operation of spin crossover in solution (Fig. 6).

The general expression of the Curie law, corrected for diamagnetism, for a mixture containing high-spin (mole fraction x_{hs}) and low-spin (mole fraction x_{ls}) complexes is given in eqn (16), where C_{hs} and C_{ls} are the Curie constants for the high-spin and low-spin forms ($C = (g^2/8)S(S+1)$ within the frame of the spin-only approximation) and TIP_{hs} and TIP_{ls} are the temperature-independent paramagnetic contributions.[39,45]

$$\chi_M^{para}T = x_{hs}\cdot(C_{hs} + T\cdot TIP_{hs}) + x_{ls}\cdot(C_{ls} + T\cdot TIP_{ls}) \quad (16)$$

The introduction of mass balance ($x_{ls} + x_{hs} = 1$) gives a straightforward access to the speciation (eqn (17) and Fig. 7).

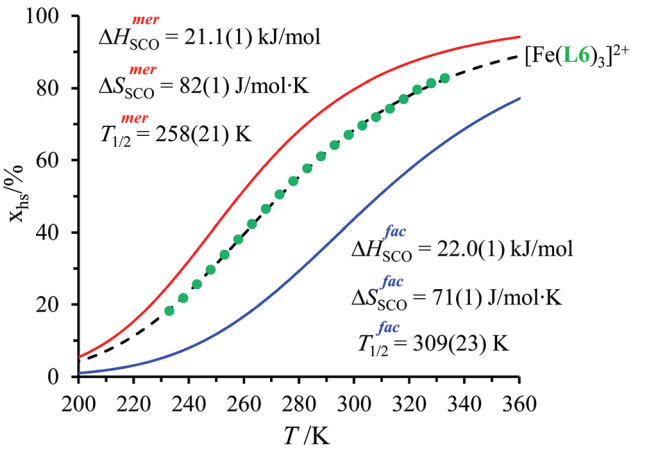

Fig. 7 Plot of high-spin mole fraction (estimated from $\chi_M^{para}T$ by using eqn (17)) *versus* temperature (T) for a 10.2 mM solution of the complex $[Fe(\mathbf{L6})_3]^{2+}$ in CD_3CN (green circles) and its analysis using eqn (20) as originating from *fac*-$[Fe(\mathbf{L6})_3]^{2+}$ (blue trace) and *mer*-$[Fe(\mathbf{L6})_3]^{2+}$ (red trace) controlled by the isomerization constant $K_{mer\rightarrow fac}^{Fe,Lk} \simeq K_{mer\rightarrow fac}^{Zn,Lk}$.

The consideration of spin-state eqn (1) eventually transforms eqn (16) into eqn (18) (see ESI Appendix 1†).[61]

$$x_{hs} = 1 - x_{ls} = \frac{\chi_M^{para}T - (C_{ls} + T\cdot TIP_{ls})}{(C_{hs} + T\cdot TIP_{hs}) - (C_{ls} + T\cdot TIP_{ls})} \quad (17)$$

$$\chi_M^{para}T = \frac{(C_{ls} - C_{hs} + T\cdot(TIP_{ls} - TIP_{hs}))}{1 + \exp\left(\frac{1}{R}\cdot\left(\Delta S_{sco} - \frac{\Delta H_{sco}}{T}\right)\right)} + C_{hs} + T\cdot TIP_{hs} \quad (18)$$

The non-linear least-square fits of the experimental paramagnetic data depicted in Fig. 6 for $[Fe(\mathbf{L6})_3]^{2+}$ and $[Fe(\mathbf{L7})_3]^{2+}$ by using eqn (18) provides Curie constants, TIP and thermodynamic parameters ΔH_{SCO} and ΔS_{SCO} for the spin crossover equilibrium gathered in Table 3 (see ESI Appendix 1 for details†).

The Curie constants C and TIP values found for $[Fe(\mathbf{L6})_3]^{2+}$ and $[Fe(\mathbf{L7})_3]^{2+}$ (Table 3, entries 5–6) are typical for the $[FeN_6]$ chromophores previously investigated in $[Fe(didentate)_3]$ complexes.[16,61,97–102] One notes that $C_{HS} > 3.00$ cm^3 K mol^{-1} (spin only value) can be taken as the signature of some partially unquenched orbital momentum in this pseudo-octahedral environment. The thermodynamic parameters $19.5 \leq \Delta H_{SCO} \leq 23$ kJ mol^{-1} and $71 \leq \Delta S_{SCO} \leq 83$ J mol^{-1} K^{-1} measured for $[Fe(\mathbf{L6})_3]^{2+}$ and $[Fe(\mathbf{L7})_3]^{2+}$ also match the usual range found for similar complexes in solution.[45,97,98] Interestingly, the pyrimidine rings in ligands **L6** and **L7** produce the weakest enthalpic change accompanying the spin crossover process in solution compared with pyridine in **L1** and pyrazine in **L4**. Due to partial H/S compensation[101–105] established for SCO processes,[105] a satisfying $\Delta H_{SCO} = \alpha\cdot\Delta S_{SCO} + \beta$ linear correlation is observed for the series of $[Fe(\mathbf{Lk})_3]^{2+}$ complexes with α = 601(103) K and β = −24 936(9020) J mol^{-1} (Fig. S35†). Consequently, the transition temperature $T_{1/2} = \Delta H_{SCO}/\Delta S_{SCO} = \alpha + (\beta/\Delta S_{SCO})$ in CD_3CN decreases with ΔS_{SCO} (since $\beta < 0$) and reaches its lowest value for $[Fe(\mathbf{L6})_3]^{2+}$ (273 K) followed by $[Fe(\mathbf{L7})_3]^{2+}$ (279 K), $[Fe(\mathbf{L1})_3]^{2+}$ (313 K) and $[Fe(\mathbf{L4})_3]^{2+}$ (351 K, Table 3, column 9).

However, the unavoidable *mer* ↔ *fac* equilibrium (14) depicted in Fig. 4 implies that the above rough analysis of the SCO processes operating in $[Fe(didentate)_3]^{2+}$ complexes in solution is of limited pertinence when the didentate ligand is non-symmetrical.[33,61] A pioneering attempt to obtain specific SCO thermodynamic contributions for *fac*-$[Fe(\mathbf{Lk})_3]^{2+}$ and *mer*-$[Fe(\mathbf{Lk})_3]^{2+}$ isomers used non-covalent lanthanide tripods to force facial arrangement around Fe^{II} as illustrated in the dimetallic triple-stranded helicate (Fig. 1). The associated thermodynamic data recorded in solution for the SCO processes occurring in LaFe-helicates, where the didentate units bound to Fe^{II} mirrors ligands **L1** and **L4**, were taken as valuable models for *fac*-$[Fe(\mathbf{Lk})_3]^{2+}$ complexes. The thermodynamic characteristics of *mer*-$[Fe(\mathbf{Lk})_3]^{2+}$ could be then deduced from the $\chi_M^{para}T$ *versus* T plots recorded for standard solution mixtures according that $K_{mer\rightarrow fac}^{Fe,Lk}$ are at hand at each temperature.[61] We propose here a parallel approach which takes reasonably for granted that the Curie constants C and the TIP contributions are identical for the *fac* and *mer* isomers of the same complex. Moreover, one also assumes (still reasonably) that

Table 3 Magnetic and thermodynamic parameters obtained from the non-linear least square fits of $\chi_M^{para}T$ *vs.* T plots recorded for $[Fe(L\boldsymbol{k})_3]^{2+}$ complexes in solution (CD_3CN)

Complex	Anion	C_{hs}/cm^3 K mol^{-1}	$TIP_{hs} \times 10^{-6}$/ cm^3 mol^{-1}	C_{ls}/cm^3 K mol^{-1}	$TIP_{ls} \times 10^{-6}$/ cm^3 mol^{-1}	ΔH_{sco}/ kJ mol^{-1}	ΔS_{sco}/ J mol^{-1} K^{-1}	$T_{1/2}$/K	Ref.
$[Fe(\mathbf{bipy})_3]^{2+}$ [a]	$CF_3SO_3^-$	—	—	0.00(8)	351(55)	—	—	—	61
$[Fe(\mathbf{L2})_3]^{2+}$ [b]	PF_6^-	3.44(2)	358(57)	—	—	—	—	—	61
$[Fe(\mathbf{L1})_3]^{2+}$	PF_6^-	3.44[c]	358[c]	0.00[c]	351[c]	28.6(3)	91.5(8)	313(4)	61
$[Fe(\mathbf{L4})_3]^{2+}$	$CF_3SO_3^-$	3.44[c]	358[c]	0.00[c]	351[c]	35.7(3)	101(1)	351(5)	61
$[Fe(\mathbf{L6})_3]^{2+}$	BF_4^-	4.10(3)	369(3)	0.00	342(3)	19.5(2)	71.3(6)	273(3)	This work
$[Fe(\mathbf{L7})_3]^{2+}$	PF_6^-	3.595(3)	368.8(2)	0.00	346.2(3)	23.01(2)	82.5(1)	279(1)	This work

[a] 100% low-spin at all studied temperatures. [b] 100% high-spin at all studied temperatures. [c] C_{ls} and TIP_{ls} found for $[Fe(\mathbf{bipy})_3]^{2+}$ and C_{hs} and TIP_{hs} found for $[Fe(\mathbf{L2})_3]^{2+}$ have been used in ref. 65 for fitting the SCO behaviors.

the thermodynamic data extracted from VT-NMR analysis for the isomerization process operating in $[Zn(L\boldsymbol{k})_3]^{2+}$ holds true for $[Fe(L\boldsymbol{k})_3]^{2+}$ (in other words $K_{mer\rightarrow fac}^{Fe,L\boldsymbol{k}}(T) \simeq K_{mer\rightarrow fac}^{Zn,L\boldsymbol{k}}(T)$). With this in mind, eqn (16) can re-written as eqn (19) and the introduction of the thermodynamic constants $K_{mer\rightarrow fac}$ and K_{SCO} finally yields eqn (20) (see ESI Appendix 2 for details†).[61]

$$\chi_M^{para}T = (x_{hs}^{fac} + x_{hs}^{mer}) \cdot (C_{hs} + T{\cdot}TIP_{hs}) + (x_{ls}^{fac} + x_{ls}^{mer}) \cdot (C_{ls} + T{\cdot}TIP_{ls}) \quad (19)$$

The different enthalpic contributions are reminiscent of the concept of *trans* influence which is thought to strengthen Fe–N bonds in the facial isomer. The entropic preference exhibited by the meridional isomer might be relevant to solvation effects. Indeed, the primary change in solvation energy accompanying the low-spin to high-spin transition is produced by the expansion of $[Fe(L\boldsymbol{k})_3]^{2+}$ considered as a charged monopole.[106,107] The associated endergonic change $\Delta\Delta_{solv}G_{monopole} \propto -(z_{hs}^2/R_{hs} - z_{ls}{}^2/R_{ls})$ modeled with Born equation[106] is expected to be very similar for both meridional and facial isomers since their cationic charges are identical

$$\chi_M^{para}T = \left(\frac{K_{SCO}^{fac\text{-}Fe(L\boldsymbol{k})_3} \cdot K_{mer\rightarrow fac}^{Fe,L\boldsymbol{k}}}{\left(1 + K_{mer\rightarrow fac}^{Fe,L\boldsymbol{k}}\right)\left(1 + K_{SCO}^{fac\text{-}Fe(L\boldsymbol{k})_3}\right)} + \frac{K_{SCO}^{mer\text{-}Fe(L\boldsymbol{k})_3}}{\left(1 + K_{mer\rightarrow fac}^{Fe,L\boldsymbol{k}}\right)\left(1 + K_{SCO}^{mer\text{-}Fe(L\boldsymbol{k})_3}\right)}\right) \cdot (C_{hs} + T \cdot TIP_{hs}) + \left(\frac{K_{mer\rightarrow fac}^{Fe,L\boldsymbol{k}}}{\left(1 + K_{mer\rightarrow fac}^{Fe,L\boldsymbol{k}}\right)\left(1 + K_{SCO}^{fac\text{-}Fe(L\boldsymbol{k})_3}\right)} + \frac{1}{\left(1 + K_{mer\rightarrow fac}^{Fe,L\boldsymbol{k}}\right)\left(1 + K_{SCO}^{mer\text{-}Fe(L\boldsymbol{k})_3}\right)}\right) \cdot (C_{ls} + T \cdot TIP_{ls}) \quad (20)$$

The systematic application of the van't Hoff relationship $\Delta G^\circ = -RT\ln(K) = \Delta H^\circ - T\Delta S^\circ$ for estimating the various stability constants together with (i) the use of $\Delta H_{mer\rightarrow fac}^{Zn,L\boldsymbol{k}}$ and $\Delta S_{mer\rightarrow fac}^{Zn,L\boldsymbol{k}}$ gathered in Table 2 for **L6** in CD_3CN and (ii) $K_{mer\rightarrow fac}^{Fe,L\boldsymbol{k}} \simeq K_{mer\rightarrow fac}^{Zn,L\boldsymbol{k}}$, allows the satisfying non-linear least-square fits with eqn (20) of $\chi_M^{para}T$ *versus* T plots for *fac*-$[Fe(\mathbf{L6})_3]^{2+}$ and *mer*-$[Fe(\mathbf{L6})_3]^{2+}$ (Fig. 7). In complete agreement with the previous analysis using a loosely constrained triple-stranded LaFe helicate for modeling *fac*-$[Fe(L\boldsymbol{k})_2]^{2+}$ ($L\boldsymbol{k}$ = **L1**, **L4**),[61] this alternative approach avoids the synthesis of the related helicates and confirms that the SCO enthalpies are only marginally larger for the facial isomer (≈1 kJ mol^{-1}). However, the SCO entropy is systematically more favorable for the meridional isomer *mer*-$[Fe(\mathbf{L6})_3]^{2+}$ by $\Delta S_{SCO}^{mer} - \Delta S_{SCO}^{fac} = 11(1)$ J mol^{-1} K^{-1}, a value mirroring those previously reported for *mer*-$[Fe(\mathbf{L1})_3]^{2+}$ (14(2) J mol^{-1} K^{-1}) and *mer*-$[Fe(\mathbf{L4})_3]^{2+}$, (11(1) J mol^{-1} K^{-1}).[61] In going from facial to meridional isomer in $[Fe(L\boldsymbol{k})_3]^{2+}$, *H*/*S* anti-compensation seems to be the rule since the spin transitions, which occur in *mer*-$[Fe(L\boldsymbol{k})_3]^{2+}$ are concomitantly favored over *fac*-$[Fe(L\boldsymbol{k})_3]^{2+}$ by (i) a lower enthalpy cost and a (ii) larger entropic gain (see Fig. 7).

($z_{hs}^{mer} = z_{hs}^{fac} = z_{ls}^{mer} = z_{ls}^{fac} = 2$) and their ionic radii are very close ($R_{fac} \approx R_{mer}$ since $V_{fac} \approx V_{mer}$). The minor, but non-negligible additional dipolar contribution to the solvation energy can be estimated with the help of *Onsager* equation to give $\Delta\Delta_{solv}G_{dipole} \propto -(\mu_{hs}{}^2/R_{i,hs}{}^3 - \mu_{ls}{}^2/R_{i,ls}{}^3)$.[108–111] Again, the radius of the spherical cavity R_i cut from the dielectric when the solute, taken as spherical, is immersed into the solvent, is similar for both isomers ($R_{i,fac} \approx R_{i,mer}$), but the magnitude of the dipole moments are different with $\mu_{fac}{}^2 > \mu_{mer}{}^2$.[112] Since $R_{i,hs} > R_{i,ls}$, then $\Delta\Delta_{solv}G_{dipole} > 0$ and the contribution of dipole solvation disfavors the low-spin to high-spin spin transition more strongly for the facial isomer than for the meridional isomer as measured by $\Delta S_{SCO}^{mer} > \Delta S_{SCO}^{fac}$.

Isolation, structures and magnetic properties of $[M(L6)_3]X_2$ and $[M(L7)_3]X_2$ in the solid state (M = Fe, Ni, Zn and X = $CF_3SO_3^-$, BF_4^-, PF_6^-, ClO_4^-)

Stoichiometric M : $L\boldsymbol{k}$ = 1 : 3 mixtures of **L6** or **L7** (10 mM) with $Ni(BF_4)_2{\cdot}6H_2O$ or $Zn(CF_3SO_3)_2$ or $Fe(ClO_4)_2{\cdot}xH_2O$ or $Fe(BF_4)_2{\cdot}6H_2O$ in acetonitrile were evaporated to dryness. The resulting microcrystalline powders were re-dissolved in acetonitrile or methanol and allowed to crystallize by evaporation,

or by diffusion of *tert*-butyl methyl ether after metathesis in presence of a large excess (10 eq.) of $(^n\mathrm{Bu})_4\mathrm{NClO_4}$ or $(^n\mathrm{Bu})_4\mathrm{NBF_4}$ or $(^n\mathrm{Bu})_4\mathrm{NPF_6}$ to give primary salts $[\mathrm{Ni}(\mathbf{L6})_3](\mathrm{BF_4})_2{\cdot}1.55\mathrm{CH_3CN}{\cdot}0.4\mathrm{H_2O}$, $[\mathrm{Zn}(\mathbf{L6})_3](\mathrm{CF_3SO_3})_2{\cdot}0.6\mathrm{H_2O}$, $[\mathrm{Fe}(\mathbf{L6})_3](\mathrm{BF_4})_2{\cdot}0.15\mathrm{CH_3CN}{\cdot}1.2\mathrm{H_2O}$, $[\mathrm{Ni}(\mathbf{L7})_3](\mathrm{BF_4})_2{\cdot}0.85\mathrm{H_2O}$, $[\mathrm{Zn}(\mathbf{L7})_3](\mathrm{PF_6})_2{\cdot}1.25\mathrm{H_2O}$, and $[\mathrm{Fe}(\mathbf{L7})_3](\mathrm{PF_6})_{1.76}(\mathrm{BF_4})_{0.24}{\cdot}0.6\mathrm{H_2O}$ complexes in 46–72% yield (Table S10†). Single crystals of sufficient quality for X-ray diffraction studies could be obtained for complexes **1–13** gathered in Fig. 8 (Tables S11–S40 and Fig. S36–S48†). Reminiscent to the empirical isolation of either pure facial or meridional isomers reported for [Fe(imidazolylimine)$_3$](Cl)(PF_6) salts with different solvent contents,[113,114] the thirteen crystal structures **1–13**, which incorporate similar $[\mathrm{M}(\mathbf{Lk})_3]^{2+}$ cations with various poorly coordinating anions and solvent molecules, are statistically partitioned between six pure facial isomers (**2**, **4**, **5**, **7**, **8**, **9**), six pure meridional isomers (**3**, **6**, **10**, **11**, **12**, **13**) and one mixture of meridional/facial (44/56%) isomers (**1**, Fig. 8 and Tables S41 and S42†). All complexes display poorly distorted octahedral [MN_6] chromophores[115] with bond lengths within the expected range.[116,117] The Fe–N bond lengths measured for $[\mathrm{Fe}(\mathbf{L6})_3](\mathrm{ClO_4})_2$ (**6**), and $[\mathrm{Fe}(\mathbf{L6})_3](\mathrm{BF_4})_2{\cdot}(\mathrm{C_5H_{12}O})_{0.5}{\cdot}(\mathrm{C_2H_5N})_{0.5}$ (**7**) at 180 K (2.03 to 2.15 Å, Table S41†) are longer than standard $\mathrm{Fe_{ls}}$–N bonds[26,38] found in $[\mathrm{Fe}(\mathbf{L7})_3](\mathrm{PF_6})(\mathrm{BF_4}){\cdot}\mathrm{CH_3OH}$ (**12**) and $[\mathrm{Fe}(\mathbf{L7})_3](\mathrm{PF_6})_{1.72}(\mathrm{ClO_4})_{0.28}{\cdot}\mathrm{CH_3OH}$ (**13**) at 150 K (1.98–1.99 Å. Table S42†). This suggests that the iron complexes with ligands **L6** exists as mixtures of low-spin and high-spin in **6** and **7** at 180 K, while those with **L7** in **12** and **13** are mainly low-spin at 150 K.

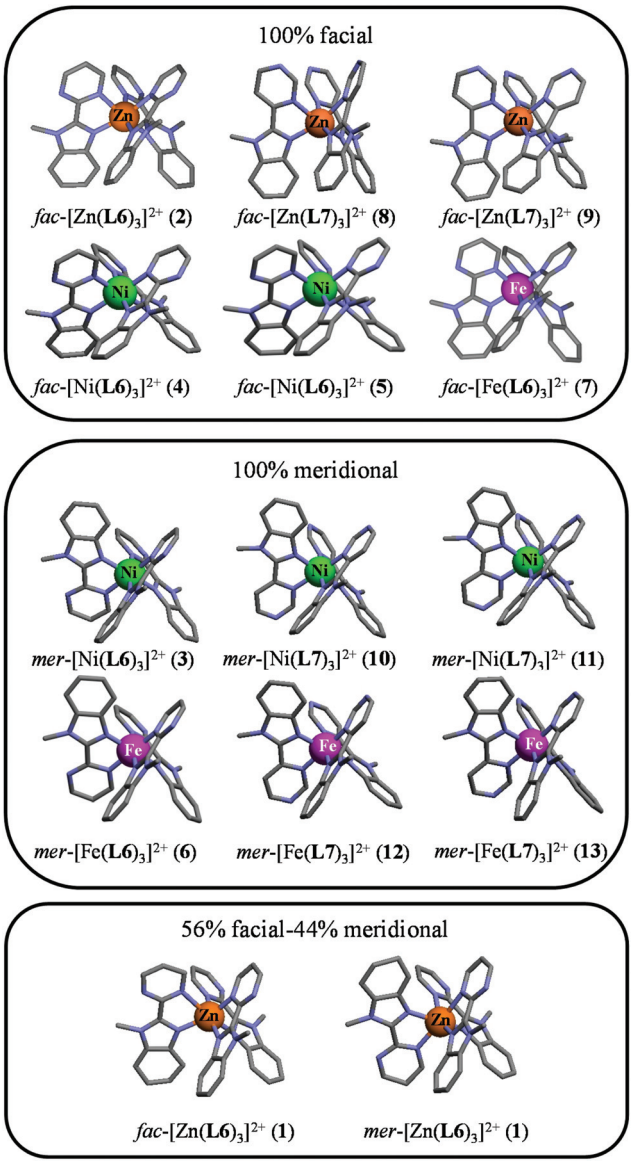

Fig. 8 Molecular structures of the $[\mathrm{M}(\mathbf{Lk})_3]^{2+}$ cations in the crystal structures of $[\mathrm{Zn}(\mathbf{L6})_3](\mathrm{ClO_4})_2(\mathrm{C_2H_3N})_{2.5}$ (**1**), $[\mathrm{Zn}(\mathbf{L6})_3](\mathrm{BF_4})_2{\cdot}(\mathrm{CH_3CN})_2$ (**2**), $[\mathrm{Ni}(\mathbf{L6})_3](\mathrm{ClO_4})_2$ (**3**), $[\mathrm{Ni}(\mathbf{L6})_3](\mathrm{ClO_4})_2{\cdot}\mathrm{C_2H_3N}$ (**4**), $[\mathrm{Ni}(\mathbf{L6})_3](\mathrm{BF_4})_2{\cdot}\mathrm{C_2H_3N}$ (**5**), $[\mathrm{Fe}(\mathbf{L6})_3](\mathrm{ClO_4})_2$ (**6**), $[\mathrm{Fe}(\mathbf{L6})_3](\mathrm{BF_4})_2{\cdot}(\mathrm{C_5H_{12}O})_{0.5}{\cdot}(\mathrm{C_2H_5N})_{0.5}$ (**7**), $[\mathrm{Zn}(\mathbf{L7})_3](\mathrm{ClO_4})_2$ (**8**) $[\mathrm{Zn}(\mathbf{L7})_3](\mathrm{PF_6})_2$ (**9**) $[\mathrm{Ni}(\mathbf{L7})_3](\mathrm{ClO_4})_{1.48}(\mathrm{PF_6})_{0.52}{\cdot}\mathrm{CH_3CN}$ (**10**), $[\mathrm{Ni}(\mathbf{L7})_3](\mathrm{BF_4})_2{\cdot}\mathrm{CH_3OH}{\cdot}(\mathrm{CH_3CN})_{0.5}$ (**11**), $[\mathrm{Fe}(\mathbf{L7})_3](\mathrm{PF_6})(\mathrm{BF_4}){\cdot}\mathrm{CH_3OH}$ (**12**) and $[\mathrm{Fe}(\mathbf{L7})_3](\mathrm{PF_6})_{1.72}(\mathrm{ClO_4})_{0.28}{\cdot}\mathrm{CH_3OH}$ (**13**).

A second collection of X-ray diffraction data at 100 K for complexes $[\mathrm{Fe}(\mathbf{L6})_3](\mathrm{ClO_4})_2$ (**6**, meridional isomer) and $[\mathrm{Fe}(\mathbf{L6})_3](\mathrm{BF_4})_2{\cdot}(\mathrm{C_5H_{12}O})_{0.5}$ (**7**, facial isomer) indeed showed a significant decrease of the Fe–N bond length, which converged to 1.99 Å at low temperature as expected for pure low-spin [FeN_6] units (Table S43†). Interestingly, complex **6** at 100 K adopts the monoclinic crystal system with one meridional isomer per asymmetric unit, and transforms into a triclinic system with two different meridional complexes (noted as Fe–A and Fe–B) per unit cell at 180 K. A careful look at the bond lengths measured in the crystal structure at 180 K (Table S25†) indeed shows different average bond lengths with 2.01(1) Å for Fe–A and 2.08(3) Å for Fe–B units. A detailed variable-temperature X-ray diffraction analysis of *mer*-$[\mathrm{Fe}(\mathbf{L6})_3]^{2+}$ in **6** revealed two successive phase transitions, monoclinic $\overset{160-170\,\mathrm{K}}{\longrightarrow}$ triclinic $\overset{240-250\,\mathrm{K}}{\longrightarrow}$ monoclinic, accompanied by a two-steps spin crossover transition (Table S44†).

Complexes Fe–B (50% of total iron content) undergo the low-spin to high-spin transition within the 165–210 K range (Fig. 9a). The remaining Fe–A sites see their coordination spheres to be slightly shrunk when low-spin Fe–B is transformed into high-spin Fe–B. Then the Fe–A sites undergo their own spin transition in the 220–250 K range (Fig. 9a). As expected, this extension of the Fe–N bond lengths is accompanied by a rather regular increase of the volume of the unit cell with small bumps at 170 and 240 K (Fig. 9b), which are confirmed by differential scanning calorimetry (Fig. S49†).

The distinction between two complex molecules with the same chemical formula, but exhibiting specific transitions in the same solid is not unprecedented and was theoretically rationalized by Sasaki and Kambara.[118] Related experimental observations of this phenomenon within the SCO topics have been reported for both Fe^{III} complexes[119] and Fe^{II} complexes,[120] which displayed an 'intermediate-phase' (IP) ordering phenomenon leading to a two-step spin-crossover behavior. The IP is defined by the limiting temperatures of the two-phase transitions and is usually formed of approximately equal proportions of LS and HS states. It is therefore not so

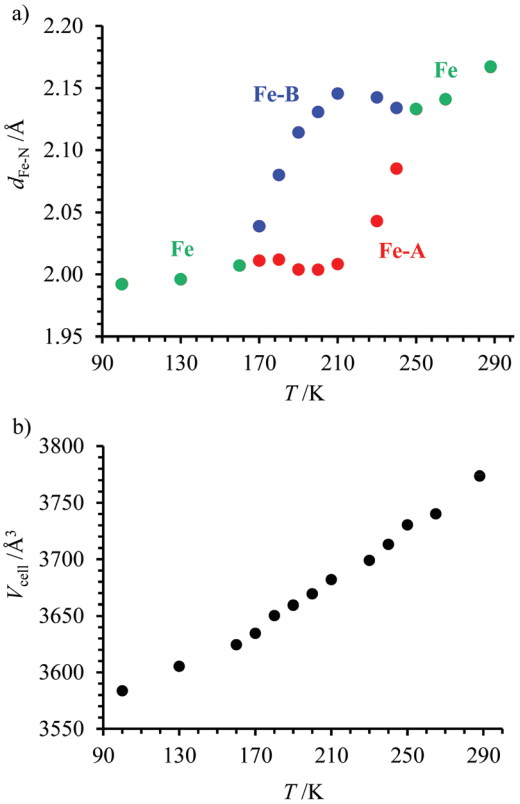

Fig. 9 Evolution of (a) Fe–N bond lengths in the monoclinic phases (green) and in the triclinic phase with Fe–A (red) and Fe–B (blue) and (b) cell volumes of $[Fe(\mathbf{L6})_3](ClO_4)_2$ (**6**) in its crystalline state as a function of temperature during heating.

surprising that paramagnetic $\chi_M^{para}T$ *versus* T plot obtained by SQUID measurements for $[Fe(\mathbf{L6})_3](ClO_4)_2$ (**6**, meridional isomers) in the solid state display two-successive spin transitions in the 100–300 K range (Fig. 10a). On the other side, $[Fe(\mathbf{L6})_3](BF_4)_2{\cdot}(C_5H_{12}O)_{0.5}$ (**7**, facial isomers) and $[Fe(\mathbf{L7})_3](PF_6)(BF_4){\cdot}CH_3OH$ (**12**, meridional isomers) exhibit regular one-step spin transitions (Fig. 10b and c). Interestingly, $[Fe(\mathbf{L6})_3](BF_4)_2{\cdot}(C_5H_{12}O)_{0.5}{\cdot}(C_2H_5N)_{0.5}$ (**7**) exhibits a complete and abrupt spin transition, which allows the reliable estimation of a Curie constant $C_{ls} = 0.0080(3)$ cm^3 K mol^{-1} and temperature-independent paramagnetism $TIP_{ls} = 387(14) \times 10^{-6}$ cm^3 mol^{-1} in the pure low-spin state and $C_{hs} = 3.53(13)$ cm^3 K mol^{-1} $TIP_{hs} = 494(18) \times 10^{-6}$ cm^3 mol^{-1} in the pure high-spin state. Taking these values as reasonable approximations for all low-spin, respectively high-spin Fe^{II} complexes with ligands **L6** and **L7**, it is possible to apply eqn (17) for transforming the plots of the molar paramagnetic susceptibility ($\chi_M T$) *versus* temperature (T) collected in Fig. 10 into plots of high-spin mole fractions (x_{hs}) as a function of temperature (Fig. S50†).

According to the various shapes observed for x_{hs} *versus* T plots (Fig. S50†), the simple van't Hoff relationship (eqn (1)) is not adequate and should be replaced with eqn (2) where the adjustable interaction parameter γ takes into account intermolecular interactions.[43,46] However, x_{hs} cannot be expressed

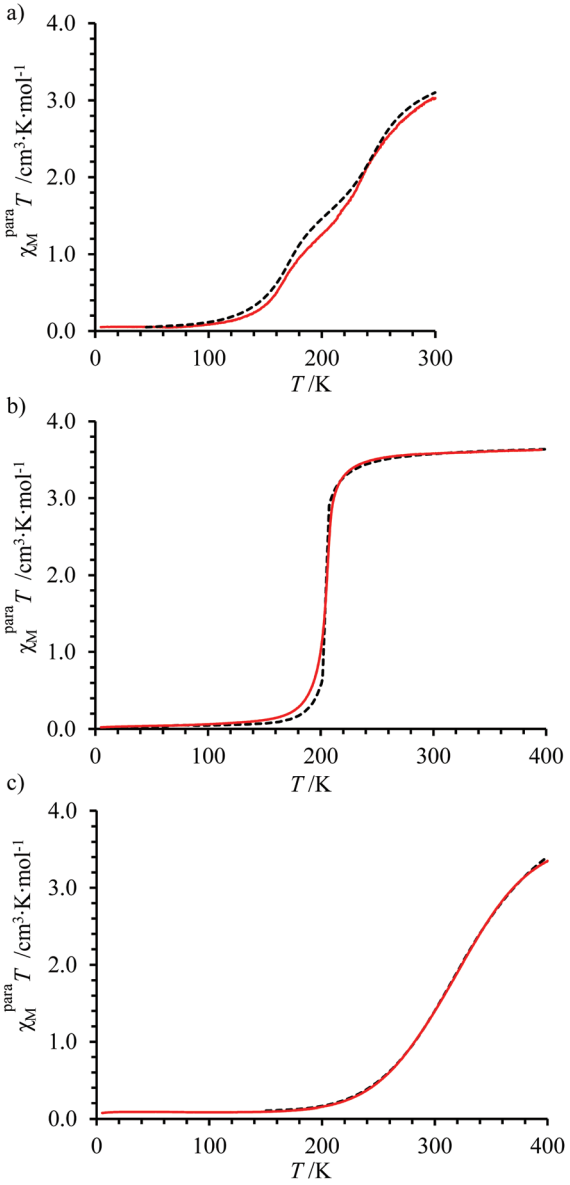

Fig. 10 Plots of molar paramagnetic susceptibility ($\chi_M T$) *versus* temperature (T) collected with increments of 1 K min^{-1} in a constant magnetic field of 5000 Oe between 5–300 K for (a) $[Fe(\mathbf{L6})_3](ClO_4)_2$ (**6**, meridional isomers) and 4–400 K for (b) $[Fe(\mathbf{L6})_3](BF_4)_2{\cdot}(C_5H_{12}O)_{0.5}$ (**7**, facial isomers) and (c) $[Fe(\mathbf{L7})_3](PF_6)(BF_4){\cdot}CH_3OH$ (**12**, meridional isomers). The red points represents the experimental data while the dashed black traces are built by using the fitted values of ΔH_{sco}, ΔS_{sco}, and γ (Table 4, see text).

analytically as a function of T with eqn (2), but the temperature can be expressed as a function of x_{hs} in eqn (21).

$$T = \frac{\Delta H_{SCO} + \gamma(1 - 2x_{hs})}{R \cdot \ln[(1 - x_{hs})/x_{hs}] + \Delta S_{SCO}} \quad (21)$$

Non-linear least squares fits using eqn (21) for the experimental $\langle T;\ x_{hs}\rangle$ couples measured for $[Fe(\mathbf{L6})_3](BF_4)_2{\cdot}(C_5H_{12}O)_{0.5}$ (**7**, facial) and $[Fe(\mathbf{L7})_3](PF_6)(BF_4){\cdot}CH_3OH$ (**12**, meridional) yield the thermodynamic constants ΔH_{sco}

Table 4 Thermodynamic parameters (ΔH_{sco}, ΔS_{sco}, and γ) associated with the SCO process in $[Fe(\mathbf{L6})_3](ClO_4)_2$ (**6**), and $[Fe(\mathbf{L6})_3](BF_4)_2{\cdot}(C_5H_{12}O)_{0.5}{\cdot}(C_2H_5N)_{0.5}$ (**7**), and $[Fe(\mathbf{L7})_3](PF_6)(BF_4){\cdot}CH_3OH$ (**12**)

Complex	$[Fe(\mathbf{L6})_3]^{2+}$ (**6**) Fe–A	Fe–B	$[Fe(\mathbf{L6})_3]^{2+}$ (**7**)	$[Fe(\mathbf{L7})_3]^{2+}$ (**12**)
Isomer	Meridional	Meridional	Facial	Meridional
ΔH_{SCO}/kJ mol^{-1}	10.6(4)	3.58(6)	15.5(9)	13.45(1)
ΔS_{SCO}/J mol^{-1} K^{-1}	42(2)	20.1(3)	75(4)	39.5(4)
$T_{1/2}$/K	251(12)	178(4)	207(16)	341(3)
γ/kJ mol^{-1}	2.54(9)	2.12(3)	3.7(2)	1.71(2)
AF[a]	4.61×10^{-3}		5.01×10^{-4}	8.51×10^{-3}

[a] Agreement factor $AF = \sqrt{\sum \left(x_{hs}^{exp} - x_{hs}^{calcd}\right)^2 / \sum \left(x_{hs}^{exp}\right)^2}$.

and ΔS_{sco} and the cooperativity factor γ collected in Table 4 (columns 4 and 5) and which satisfyingly reproduce the experimental data (Fig. 10b, c and S50b, c†).

Since the energies of intermolecular interactions overpass those induced by the molecular SCO processes, ΔH_{sco}, ΔS_{sco} observed in the solid state for $[Fe(\mathbf{L6})_3](BF_4)_2{\cdot}(C_5H_{12}O)_{0.5}{\cdot}(C_2H_5N)_{0.5}$ (**7**), and $[Fe(\mathbf{L7})_3](PF_6)(BF_4){\cdot}CH_3OH$ (**12**, Table 4) significantly deviate from those recorded in solution (Table 3). Consequently, the transition temperature found for *fac*-$[Fe(\mathbf{L6})]^{2+}$ in acetonitrile ($T_{1/2}$ = 309(23) K in Fig. 7) does not match that found in the crystal structure of **7** ($T_{1/2}$ = 207(16) K). The systematic operation of positive cooperativity observed for $[Fe(\mathbf{L6})_3](BF_4)_2{\cdot}(C_5H_{12}O)_{0.5}$ (**7**, γ = 3.7(2) kJ mol^{-1}), and $[Fe(\mathbf{L7})_3](PF_6)(BF_4){\cdot}CH_3OH$ (**12**, γ = 1.71(2) kJ mol^{-1}) in the solid state is more instructive and suggests that these crystal lattices are well-adapted for accommodating the larger high-spin form. The value of γ found for **7** in the solid state is slightly larger than $2RT_{1/2}$ ($\gamma > 2RT_{1/2}$ = 3.4 kJ mol^{-1}) and we must consider the possibility that the latter complex might undergo a hysteretic transition between the low-spin and the high-spin states.[39,40] However, the record of magnetic susceptibility along a complete heating and cooling cycle showed no interpretable hysteresis, but some drift resulting from the evaporation of volatile interstitial solvent molecules (Fig. S51†).

Finally, molar magnetic susceptibilities (χ_M^{para}) recorded for *mer*-$[Fe(\mathbf{L6})_3](ClO_4)_2$ (**6**) at variable temperatures between 5–300 K indeed confirmed the crystallographic studies and the operation of two successive SCO transitions, each affecting 50% of the total iron complexes (Fig. 10a). The magnetic data could be rationalized with eqn (22), which considers an equimolar mixture of two complexes Fe–A ($T_{1/2}$ at high temperature) and Fe–B ($T_{1/2}$ at low temperature) in the solid state.

$$2\chi_M T = \sum_{i=A,B} \left[x_{hs}^i \cdot \left(C_{hs}^i + T \cdot TIP_{hs}^i\right) + \left(1 - x_{hs}^i\right) \cdot \left(C_{ls}^i + T \cdot TIP_{ls}^i\right)\right] \quad (22)$$

Introducing the single set of magnetic parameter C_{ls} = 0.008 cm^3 K mol^{-1}, C_{hs} = 3.53 cm^3 K mol^{-1}, $TIP_{ls} = 387 \times 10^{-6}$ cm^3 mol^{-1} and $TIP_{hs} = 494 \times 10^{-6}$ cm^3 mol^{-1} into eqn (22) transforms the experimental $\chi_M T$ values recorded for *mer*-$[Fe(\mathbf{L6})_3](ClO_4)_2$ (**6**, Fig. 10a) into total high-spin mole fractions $x_{hs}^{tot} = x_{hs}^A + x_{hs}^B$ (Fig. S50a†). Assuming that the growth of high-spin fraction is solely assigned to x_{hs}^B in the 140–200 K range and to x_{hs}^A in the 225–300 K domain allows two separated non-linear least-square fits of the $\langle T; x_{hs}\rangle$ couples with eqn (21) for the two successive transitions detected in *mer*-$[Fe(\mathbf{L6})_3](ClO_4)_2$ (**6**, Fig. 10a). The associated approximated thermodynamic parameters are collected in Table 4 (columns 2 and 3) and show transition temperatures $T_{1/2}$(Fe–B) = 178(4) K and $T_{1/2}$(Fe–A) = 251(12) K in line with the phase transition observed by DSC (Fig. S48,† $T_{1/2}$ = 167 K and 241 K). Some slight positive cooperativity $2.1 \leq \gamma \leq 2.5$ kJ mol^{-1} operates within each spin state transition in *mer*-$[Fe(\mathbf{L6})_3](ClO_4)_2$ (**6**) and, as expected from the very limited cooperativity factors, the $\chi_M^{para}T$ *versus* T plots recorded for **6** and **12** for heating–cooling cycles show no hysteresis.

Conclusion

Even if it may appear tedious, there is currently no more efficient method to tune SCO properties of a $[FeN_6]$ unit than the use of some semi-empirical trial/analysis/optimization procedures within a family of closely related complexes as proposed for the **L1–L7** series. In this context, $[Fe(\mathbf{L6})_3]^{2+}$ emerges to be the best candidate in term of both stability and spin transition temperature in solution, to be connected to luminescent lanthanide stains in metallosupramolecular architectures. These systematic studies (i) confirmed the unpredictability of SCO behaviors and associated thermodynamic parameters observed in solid state materials, and (ii) allowed us to focus our attention on the effect of *mer* ↔ *facial* isomerization on the spin state transitions operating for $[Fe(didentate)_3]^{2+}$ in solution (didentate stands for a non-symmetrical diimine ligand). As expected from the minor thermodynamic *trans* influence reported for the formation of pseudo-octahedral complexes along the 3d series,[74,84] ΔH_{SCO} are slightly more positive, and thus unfavourable, for the facial isomers ($\Delta H_{SCO}^{fac} - \Delta H_{SCO}^{mer} \approx 1$ kJ mol^{-1}). This trend is amplified by a larger drift originating from an entropic preference for SCO operating in the meridional isomers in solution $\Delta S_{SCO}^{mer} - \Delta S_{SCO}^{fac} \approx 11$ J mol^{-1} K^{-1}. Since the same entropic gap has been previously reported in triple-stranded FeLn helicates, where the facial isomer is prevented to transform into meridional isomer by the non-covalent lanthanide tripod,[61] we conclude that, in

solution, *mer*-$[Fe_{hs}(didentate)_3]^{2+}$ is systematically entropically favored over *fac*-$[Fe_{hs}(didentate)_3]^{2+}$ by dipolar solvation effects. With the [Fe(2-pyrimidine-benzimidazole)$_3$] units as programmed in $[Fe(\mathbf{L6})_3]^{2+}$, we are now equipped for the exploration of dinuclear Fe^{II}–Ln^{III} complexes, the lanthanide-based luminescence of which could be modulated by Fe^{II} spin crossover at the molecular level.

Experimental section

General

Chemicals were purchased from Sigma-Aldrich and Acros and used without further purification unless otherwise stated. Dichloromethane, 1,2-dichloroethane, *tert*-butyl methyl ether and *N*,*N*-dimethylformamide were dried through an alumina cartridge. Silica-gel plates (Merck, 60 F_{254}) were used for thin-layer chromatography, SiliaFlash® silica gel P60 (0.04–0.063 mm), and Acros silica gel 60 (0.035–0.07 mm) were used for preparative column chromatography.

Preparation of pyrimidine-2-carboxylic acid (1)

Pyrimidine-2-carboxylic acid was synthesized according to a slightly modified reported procedure.[121] Pyrimidine-2-carbonitrile (5.02 g, 47.76 mmol, 1 eq.) was stirred with 5 M NaOH (35 mL) at 55 °C for 3 h. The solution was neutralized (pH 2.0) with diluted aqueous HCl and evaporated to dryness. The resulting solid was suspended in acetonitrile, refluxed for 1 h, and filtered when hot to remove the insoluble salts. The filtrate was evaporated under vacuum to dryness. The resulting solid was re-dissolved in methanol and crystallized to give 3.21 g of pyrimidine-2-carboxylic acid (**2**, 25.8 mmol, yield 54%) as colourless thin needles. ^{1}H NMR ($CDCl_3$, 400 MHz, 298 K) δ/ppm: 7.61 (1H, t, ^3J = 4.9 Hz), 9.00 (2H, d, ^3J = 4.9 Hz), 10.62 (br).

Preparation of *N*-methyl-2-nitroaniline (2)

1-Chloro-2-nitrobenzene (30 g, 190.4 mmol, 1 eq.) and methylamine (197.7 mL 40% wt. in water, 2.28 mol, 12 eq.) were introduced into a Carius tube equipped with a magnetic stirrer and heated at 120 °C for 48 h. The excess of methylamine was rotary evaporated, and the residual brown oil was partitioned between CH_2Cl_2 (300 mL) and half-saturated aqueous NH_4Cl (300 mL). The organic layer was separated and the aqueous phase was further extracted with CH_2Cl_2 (3 × 150 mL). The combined organic extracts were dried over anhydrous Na_2SO_4, filtered and the solvent evaporated to dryness. The resulting red oil was purified by column chromatography (silica, CH_2Cl_2) to give *N*-methyl-2-nitroaniline (**1**, 178.57 mmol, yield 94%) as a deep red/orange oil, which was crystallized upon trituration. ^{1}H NMR ($CDCl_3$, 400 MHz, 298 K) δ/ppm = 8.13 (1 H, dd, ^3J = 8.8 Hz, ^4J = 1.6 Hz), 8.00 (1 H, bs), 7.43 (1 H, ddd, ^3J = 8.8 Hz, ^3J = 7.2 Hz, ^4J = 1.6 Hz), 6.81 (1 H, dd, ^3J = 8.6 Hz, ^4J = 1.0 Hz), 6.62 (1 H, ddd, ^3J = 8.4 Hz, ^3J = 7.2 Hz, ^4J = 1.2 Hz), 2.99 (3 H, s).

Preparation of *N*-methyl-*N*-(2-nitrophenyl)pyrimidine-2-carboxamide (3)

Thionyl chloride (7.41 mL, 12.15 g, 102.14 mmol, 9.26 eq.) was added dropwise to the mixture of pyrimidine-2-carboxylic acid (**1**, 1.37 g, 11.03 mmol, 1 eq.) dissolved dry 1,2-dichloroethane (35 mL). Dimethylformamide (300 μL) was added to the reaction mixture. The solution was refluxed for 5 h under an inert atmosphere of nitrogen, then cooled and evaporated to dryness. The residue was dissolved in 40 mL of dry 1,2-dichloroethane. *N*-Methyl-2-nitroaniline (**2**, 4.19 g, 27.57 mmol, 2.5 eq.) dissolved in 10 mL 1,2-dichloroethane was added dropwise to the solution. The solution was refluxed 15 h during which two portions of $(iPr)_2NEt$ (Hünig's base, 3.5 mL, 20.09 mmol, 1.82 eq.) were added after 30 min and 12 h. The solution was concentrated under vacuum to afford a solid residue which was partitioned between CH_2Cl_2 (400 mL) and half saturated aqueous NH_4Cl (4 × 120 mL). The aqueous phase was further extracted with CH_2Cl_2 (3 × 50 mL). The combined organic phase was dried over anhydrous Na_2SO_4, concentrated under vacuum and purified by column chromatography (silica, CH_2Cl_2/MeOH 99.2 : 0.8) to give 2.62 g of *N*-methyl-*N*-(2-nitrophenyl)pyrimidine-2-carboxamide (**3**, 10.14 mmol, yield 92%) as a beige solid. ^{1}H NMR ($CDCl_3$, 400 MHz, 298 K) δ/ppm: mixture of rotamers A (86.5%) and B (13.5%): 3.41 (3H, s, B), 3.55 (3H, s, A), 7.08–7.75 (4H, m, A and B), 7.95 (1H, dd, ^3J = 8.4 Hz, A), 8.10 (1H, dd, ^3J = 8.6 Hz, B), 8.53 (2H, d, ^3J = 4.8 Hz, A), 8.91 (2H, d, ^3J = 4.9 Hz, B). ESI-MS (soft positive mode – MeOH + $CHCl_3$ + HCOOH)- $[\mathbf{3} + H]^+$ = 259.3 (exp.) 259.3 (calc.), $[\mathbf{3} + Na]^+$ = 281.4 (exp.) 281.2 (calc.), 213.4, 136.4, 119.3, 107.3 (fragments).

Preparation of 1-methyl-2-(pyrimidin-2-yl)-1*H*-benzo[*d*]imidazole (L6)

N-Methyl-*N*-(2-nitrophenyl)pyrimidine-2-carboxamide (**3**, 2.60 g, 10.06 mmol, 1 eq.) was dissolved in a mixture of EtOH : DMF (20 mL : 25 mL). Sodium dithionite (7 g, 40.20 mmol, 3.97 eq.) was added to the solution and the temperature of the mixture was raised to 60 °C when 20 mL of distilled water was added. After refluxing for 24 h, the mixture was neutralized using aqueous ammonia and the solvents were removed *in vacuo*. The concentrate was dissolved in CH_2Cl_2 (50 mL) and washed with water (3 × 200 mL). The aqueous layers were collectively re-extracted with CH_2Cl_2 (3 × 50 mL). The combined organic fractions were then concentrated under vacuum and purified by column chromatography (silica, CH_2Cl_2/MeOH 98 : 2) to yield **L6** (5.86 mmol, yield 58%). The compound was crystallized as needles by slow diffusion of *n*-hexane into CH_2Cl_2. ^{1}H-NMR (CD_3CN, 400 MHz, 298 K) δ/ppm; 4.175 (3H, s), 7.29–7.33 (1H, ddd, ^3J = 5.4–8.1 Hz, ^4J = 1.2 Hz), 7.37–7.41 (1H, ddd, ^3J = 6.8–8.2 Hz, ^4J = 1.2 Hz), 7.47 (1 H, t, ^3J = 4.8 Hz), 7.57 (1 H, ddd, ^3J = 8.1 Hz, ^4J = 0.9 Hz), 7.78 (1 H, ddd, ^3J = 8.0 Hz, ^4J = 0.8 Hz), 8.95 (2 H, d, ^3J = 4.8 Hz). ^{13}C-NMR (CD_3CN, 101 MHz, 298 K) δ/ppm; 159.59 (C_q), 158.48 (CH), 150.33 (C_q), 143.59 (C_q), 138.12 (C_q), 124.72 (CH), 123.46 (CH), 121.81 (CH), 121.27 (CH), 111.67 (CH),

33.28 (CH_3). ESI-MS (soft positive mode – MeOH + $CHCl_3$ + HCOOH): [**L6** + H]$^+$ = 211.3 (exp.) 211.09 (calc.), [**L6** + Na]$^+$ = 233.1 (exp.) 233.08 (calc.), 170.3 (fragments). Elemental analysis: calculated (%): C 68.56, H 4.79, N 26.65; found (%): C 68.39, H 4.69, N 26.82.

Preparation of *N*-methyl-*N*-(2-nitrophenyl)pyrimidine-4-carboxamide (4)

Oxalyl chloride (55.33 mL, 14.0 g, 110.3 mmol, 10 eq.) was added dropwise to a mixture of pyrimidine-2-carboxylic acid (1.37 g, 11.03 mmol, 1 eq.) dissolved in dry dichloromethane (35 mL). Dimethylformamide (300 μL) was added to the mixture to catalyze the reaction. The solution was refluxed for 2 h under an inert atmosphere of nitrogen, then cooled and evaporated to dryness. The residue was dissolved in 40 mL of dry dichloromethane. *N*-Methyl-2-nitroaniline (**2**, 4.19 g, 27.57 mmol, 2.5 eq.) dissolved in 10 mL dichloromethane was added dropwise to the solution. The solution was refluxed for 15 h during which two portions of $(iPr)_2NEt$ (Hünig's base, 3.5 mL, 20.09 mmol, 1.82 eq.) were added after 30 min and 12 h. The solution was concentrated under vacuum to afford a solid residue which was partitioned between CH_2Cl_2 (400 mL) and half saturated aqueous NH_4Cl (4 × 120 mL). The aqueous phase was further extracted with CH_2Cl_2 (3 × 50 mL). The combined organic phase was dried over anhydrous Na_2SO_4, concentrated under vacuum and purified by column chromatography (silica, CH_2Cl_2/MeOH 99 : 1) to give 2.62 g of *N*-methyl-*N*-(2-nitrophenyl)pyrimidine-4-carboxamide (**4**, 8.34 mmol, yield 76%) as a brown viscous liquid. ^{1}H NMR ($CDCl_3$, 400 MHz, 298 K) δ/ppm: mixture of rotamers A (15.1%) and B (84.9%): 3.49 (3H, s, B), 3.52 (3H, s, A), 7.34–7.77 (4H, m, A and B), 7.95 (1H, dd, ^3J = 8.2 Hz, ^4J = 1.4 Hz, B), 8.11 (1H, dd, ^3J = 8.1 Hz, ^4J = 1.1 Hz, A), 8.75 (1H, d, ^3J = 5.1 Hz, B), 8.95 (1H, d, ^3J = 5.0 Hz, A), 8.78 (1H, d, ^3J = 1.2 Hz, B), 9.33 (1H, A). ESI-MS (soft positive mode – MeOH + $CHCl_3$ + HCOOH): [**4** + H]$^+$ = 259.3 (exp.) 259.3 (calc.), [**4** + Na]$^+$ = 281.3 (exp.) 281.2 (calc.), 213.4, 184.3, 136.3, 119.3, 108.3 (fragments).

Preparation of 1-methyl-2-(pyrimidin-4-yl)-1*H*-benzo[*d*]imidazole (L7)

N-Methyl-*N*-(2-nitrophenyl)pyrimidine-4-carboxamide (**4**, 2.60 g, 10.06 mmol, 1 eq.) was dissolved in EtOH : DMF (20 mL : 25 mL). Sodium dithionite (7 g, 40.20 mmol, 3.97 eq.) was added to the solution and the temperature of the mixture was raised to 60 °C when 20 mL of distilled water was added. After refluxing for 24 h, the mixture was neutralized using aqueous ammonia and the solvents were removed *in vacuo*. The concentrate was dissolved in CH_2Cl_2 (50 mL) and washed with water (3 × 200 mL). The combined aqueous layers were extracted with CH_2Cl_2 (3 × 50 mL). The organic fraction was then concentrated under vacuum and purified by column chromatography (silica, CH_2Cl_2/MeOH 98.5 : 1.5) to yield **L7** (5.21 mmol, yield 52%). The compound was crystallized as needles by slow diffusion of *n*-hexane into CH_2Cl_2. ^{1}H-NMR (CD_3CN, 400 MHz, 298 K) δ/ppm; 4.31 (3H, s), 7.33 (1H, ddd, ^4J = 1.2 Hz, ^3J = 7.9 Hz), 7.41 (1H, ddd, ^4J = 1.2 Hz, ^3J = 8.0 Hz), 7.59 (1H, dt, ^4J = 1 Hz, ^3J = 8.2 Hz), 7.76 (1H, dt, ^4J = 1 Hz, ^3J = 8.1 Hz), 8.32 (1H, dd, ^4J = 1.6 Hz, ^3J = 5.2 Hz), 8.89 (1H, d, ^3J = 5.2 Hz), 9.28 (1H, d, ^4J = 1.6 Hz). ^{13}C-NMR (CD_3CN, 101 MHz, 298 K) δ/ppm; 158.99 (CH), 158.38 (C_q), 148.79 (C_q), 143.51 (C_q), 138.73 (C_q), 125.13 (CH), 123.82 (CH), 121.38 (CH), 121.03 (CH), 111.78 (CH), 33.54 (CH_3). ESI-MS (soft positive mode – MeOH + $CHCl_3$ + HCOOH) [**L7** + H]$^+$ = 210.6 (exp.) 211.09 (calc.), [**L7** + Na]$^+$ = 233.1 (exp.) 233.08 (calc.), 82.4 (fragments). Elemental analysis: calculated (%): C 68.56, H 4.79, N 26.65; found (%): C 68.32, H 4.72, N 27.00.

Preparation $[M(L6)_3]X_2$ and $[M(L7)_3]X_2$ complexes (M = Fe, Ni, Zn and X = $CF_3SO_3^-$, BF_4^-, PF_6^-, ClO_4^-)

In a typical synthesis, 0.3 mmol (3 eq.) of the ligand **L6** or ligand **L7** dissolved in 2 mL of acetonitrile was added to 0.1 mmol (1 eq.) of $Ni(BF_4)_2{\cdot}6H_2O$ or $Zn(CF_3SO_3)_2$ or $Fe(ClO_4)_2{\cdot}xH_2O$ or $Fe(BF_4)_2{\cdot}6H_2O$ in 2 mL acetonitrile. The resulting mixtures were stirred under an inert atmosphere for 3 h for ensuring complete dissolution of all components and then evaporated to dryness to yield microcrystalline powders of the respective complexes. The powders were re-dissolved in acetonitrile or methanol and allowed to crystallize by evaporation, or diffusion of *tert*-butyl methyl ether into acetonitrile or methanol after metathesis in presence of a large excess (10 eq.) of $(^nBu)_4NClO_4$, $(^nBu)_4NBF_4$ or $(^nBu)_4NPF_6$, respectively, to give primary salts $[Ni(\mathbf{L6})_3](BF_4)_2{\cdot}1.55CH_3CN{\cdot}0.4H_2O$, $[Zn(\mathbf{L6})_3](CF_3SO_3)_2{\cdot}0.6H_2O$, $[Fe(\mathbf{L6})_3](BF_4)_2{\cdot}0.15CH_3CN{\cdot}1.2H_2O$, $[Ni(\mathbf{L7})_3](BF_4)_2{\cdot}0.85H_2O$, $[Zn(\mathbf{L7})_3](PF_6)_2{\cdot}1.25H_2O$, $[Fe(\mathbf{L7})_3](PF_6)_{1.76}(BF_4)_{0.24}{\cdot}0.6H_2O$ complexes in 46–72% yield. Only non-perchlorate complexes were characterized by elemental analyses (Table S10†). Single crystals of sufficient quality for X-ray diffraction studies could be obtained and X-ray crystal structures could be solved for $[Zn(\mathbf{L6})_3](ClO_4)_2(C_2H_3N)_{2.5}$ (**1**), $[Zn(\mathbf{L6})_3](BF_4)_2{\cdot}(CH_3CN)_2$ (**2**), $[Ni(\mathbf{L6})_3](ClO_4)_2$ (**3**), $[Ni(\mathbf{L6})_3](ClO_4)_2{\cdot}C_2H_3N$ (**4**), $[Ni(\mathbf{L6})_3](BF_4)_2{\cdot}C_2H_3N$ (**5**), $[Fe(\mathbf{L6})_3](ClO_4)_2$ (**6**), $[Fe(\mathbf{L6})_3](BF_4)_2{\cdot}(C_5H_{12}O)_{0.5}{\cdot}(C_2H_5N)_{0.5}$ (**7**), $[Zn(\mathbf{L7})_3](ClO_4)_2$ (**8**) $[Zn(\mathbf{L7})_3](PF_6)_2$ (**9**) $[Ni(\mathbf{L7})_3](ClO_4)_{1.48}(PF_6)_{0.52}{\cdot}CH_3CN$ (**10**), $[Ni(\mathbf{L7})_3](BF_4)_2{\cdot}CH_3OH{\cdot}(CH_3CN)_{0.5}$ (**11**), $[Fe(\mathbf{L7})_3](PF_6)(BF_4){\cdot}CH_3OH$ (**12**) and $[Fe(\mathbf{L7})_3](PF_6)_{1.72}(ClO_4)_{0.28}{\cdot}CH_3OH$ (**13**).

Caution! Dry perchlorates may explode and should be handled in small quantities and with the necessary precautions.[122,123]

Spectroscopic and analytical measurements

^{1}H, ^{13}C NMR and ^{1}H–^{15}N HMBC spectra were recorded at 298 K on a Bruker Avance 400 MHz spectrometer. Chemical shifts are given in ppm with respect to TMS for ^{1}H and ^{13}C and nitromethane for ^{15}N. Spectrophotometric titrations were performed with a J&M diode array spectrometer (Tidas series) connected to an external computer. In a typical experiment, 25 cm^3 of ligand **L6** or ligand **L7** in acetonitrile (~2 × 10^{-4} M) was titrated at 298 K with a solution of $Fe(CF_3SO_3)_2$ and $Ni(BF_4)_2{\cdot}6H_2O$ or $Zn(CF_3SO_3)_2$ (~2 × 10^{-3} M) in acetonitrile under an inert atmosphere. After each addition of 33 μL, the absorbance was recorded using Hellma optrodes (optical path length 0.1 cm) immersed in the thermostated titration vessel and connected to the spectrometer. Mathematical treatment of

the spectrophotometric titrations was performed with factor analysis[67–69] and with ReactLab™ Equilibria (previously Specfit/32).[69,71,72] Pneumatically-assisted electrospray (ESI-MS) mass spectra were recorded from ~1×10^{-4} M (ligands) and ~1×10^{-3} M (complexes) solutions on an Applied Biosystems API 150EX LC/MS System equipped with a Turbo Ionspray source. Elemental analyses were performed by K. L. Paglia from the Microchemical Laboratory of the University of Geneva. Electronic spectra in the UV-Vis region were recorded at 293 K from solutions in CH_3CN with a PerkinElmer Lambda 1050 using quartz cells of 0.1 or 1.0 mm path length. Solid-state absorption spectra were recorded with a PerkinElmer Lambda 900 using capillaries. Solid-state magnetic data were recorded on MPMS 3 QUANTUM DESIGN magnetometers using magnetic fields of 1000–5000 Oe and at 1 K min^{-1} rates within the 5–400 K range (5–300 K range for perchlorate containing complexes). The magnetic susceptibilities were corrected for the magnetic response of the sample holder and the diamagnetism of the compounds by using the approximation $\chi_D = -\frac{MW}{2} \times 10^{-6}$ emu mol^{-1}.[124]

X-ray crystallography

Summary of crystal data, intensity measurements and structure refinements for ligands **L6**, **L7** and complexes $[Zn(\mathbf{L6})_3](ClO_4)_2(C_2H_3N)_{2.5}$ (**1**), $[Zn(\mathbf{L6})_3](BF_4)_2\cdot(CH_3CN)_2$ (**2**), $[Ni(\mathbf{L6})_3](ClO_4)_2$ (**3**), $[Ni(\mathbf{L6})_3](ClO_4)_2\cdot C_2H_3N$ (**4**), $[Ni(\mathbf{L6})_3](BF_4)_2\cdot C_2H_3N$ (**5**), $[Fe(\mathbf{L6})_3](ClO_4)_2$ (**6**), and $[Fe(\mathbf{L6})_3](BF_4)_2\cdot(C_5H_{12}O)_{0.5}\cdot(C_2H_5N)_{0.5}$ (**7**), $[Zn(\mathbf{L7})_3](ClO_4)_2$ (**8**) $[Zn(\mathbf{L7})_3](PF_6)_2$ (**9**) and $[Ni(\mathbf{L7})_3](ClO_4)_{1.48}(PF_6)_{0.52}\cdot CH_3CN$ (**10**), $[Ni(\mathbf{L7})_3](BF_4)_2\cdot CH_3OH\cdot(CH_3CN)_{0.5}$ (**11**), $[Fe(\mathbf{L7})_3](PF_6)(BF_4)\cdot CH_3OH$ (**12**) and $[Fe(\mathbf{L7})_3](PF_6)_{1.72}(ClO_4)_{0.28}\cdot CH_3OH$ (**13**) were collected in Tables S1, S4 and S8–S11.† Pertinent bond lengths, bond angles and interplanar angles were collected in Tables S2, S3, S5, S6, S15–S40† together with ORTEP views and the pertinent numbering schemes and intermolecular interactions gathered in Fig. S15–S20 and S36–S48.† The crystals were mounted on Hampton cryoloops with protection oil. X-ray data collections were performed with an Agilent SuperNova Dual diffractometer equipped with a CCD Atlas detector (Cu[Kα] radiation) or a XtaLAB Synergy-S diffractometer equipped with an hybrid pixel hypix arc 150 detector. The structures were solved by using direct methods.[125,126] Full-matrix least-square refinements on F^2 were performed with SHELX2014.[127] CCDC 2041614–2041630† contain the supplementary crystallographic data.

Conflicts of interest

There are no conflicts to declare.

Acknowledgements

Financial support from the Swiss National Science Foundation is gratefully acknowledged (grant numbers: 200020_178758 and 206021_183324).

References

1 L. Pauling, *J. Am. Chem. Soc.*, 1931, **53**, 1367–1400.
2 L. Pauling, *Phys. Rev.*, 1931, **37**, 1185–1186.
3 L. Pauling, *J. Am. Chem. Soc.*, 1932, **54**, 988–1003.
4 C. D. Corryell, F. Stittand and L. Pauling, *J. Am. Chem. Soc.*, 1937, **59**, 633–642.
5 L. Cambi and L. Szego, *Ber. Dtsch. Chem. Ges.*, 1931, **64**, 2591–2598.
6 L. Cambi, L. Szego and A. Cagnasso, *Atti Accad. Lincei*, 1932, **15**, 266–271.
7 L. Cambi, L. Szego and A. Cagnasso, *Atti Accad. Lincei*, 1932, **15**, 329–335.
8 H. Bethe, *Ann. Phys.*, 1929, **3**, 133–208.
9 C. K. Jorgensen, *Modern Aspects of Ligand Field Theory*, North Holland Publishing Company, Amsterdam-London, 1971.
10 B. N. Figgis and M. A. Hitchman, *Ligand Field Theory and Its Applications*, Wiley-VCH, New York, Chichester, Weiheim, Brisbane, Singapore, Toronto, 2000.
11 D. M. P. Mingos, *Struct. Bonding*, 2016, **172**, 1–18.
12 A. Hauser, *Top. Curr. Chem.*, 2004, **233**, 49–58.
13 Y. Tanabe and S. Sugano, *J. Phys. Soc. Jpn.*, 1954, **9**, 766–779.
14 P. Gütlich, Y. Garcia and H. A. Goodwin, *Chem. Soc. Rev.*, 2000, **29**, 419–427.
15 S. Alvarez, *J. Am. Chem. Soc.*, 2003, **125**, 6795–6802.
16 N. Deorukhkar, T. Lathion, L. Guénée, C. Besnard and C. Piguet, *Chemistry*, 2020, **2**, 231–252.
17 R. J. Deeth, C. M. Handley and B. J. Houghton, in *Spin-Crossover Materials*, ed. M. A. Halcrow, Wiley, Chichester, 2013, vol. 17, pp. 443–454.
18 F. Neese, *Coord. Chem. Rev.*, 2009, **253**, 526–563.
19 C. J. Cramer and D. G. Truhlar, *Phys. Chem. Chem. Phys.*, 2009, **11**, 10757–10816.
20 S. Rackwitz, W. Klopper, V. Schünemann and J. A. Wolny, *Phys. Chem. Chem. Phys.*, 2013, **15**, 15450–15458.
21 L. J. K. Cook, R. Kulmaczewski, R. Mohammed, S. Dudley, S. A. Barrett, M. A. Little, R. J. Deeth and M. A. Halcrow, *Angew. Chem., Int. Ed.*, 2016, **55**, 4327–4331.
22 K. P. Kepp, *Inorg. Chem.*, 2016, **55**, 2717–2727.
23 M. Swart and M. Gruden, *Acc. Chem. Res.*, 2016, **49**, 2690–2697.
24 S. Rodriguez-Jimenez, M. Yang, I. Stewart, A. L. Garden and S. Brooker, *J. Am. Chem. Soc.*, 2017, **139**, 18392–18396.
25 P. Gütlich and H. A. Goodwin, *Top. Curr. Chem.*, 2004, **233**, 1–47.
26 M. A. Halcrow, *Polyhedron*, 2007, **26**, 3523–3576.
27 B. Weber, in *Spin-Crossover Materials*, ed. M. A. Halcrow, Wiley, Chichester, 2013, vol. 2, pp. 55–76.
28 J. Olguin and S. Brooker, in *Spin-Crossover Materials*, ed. M. A. Halcrow, Wiley, Chichester, 2013, vol. 3, pp. 77–120.
29 J. Olguin and S. Brooker, *Coord. Chem. Rev.*, 2011, **255**, 203–240.
30 S. Brooker, *Chem. Soc. Rev.*, 2015, **44**, 2880–2892.
31 H. L. C. Feltham, A. S. Barltrop and S. Brooker, *Coord. Chem. Rev.*, 2016, **344**, 26–53.

32 R. W. Hogue, S. Singh and S. Brooker, *Chem. Soc. Rev.*, 2018, **47**, 7303–7338.
33 H. S. Scott, R. W. Staniland and P. E. Kruger, *Coord. Chem. Rev.*, 2018, **362**, 24–43.
34 K. S. Kumar, Y. Bayeh, T. Gebretsadik, F. Elemo, M. Gebrezgiabher, M. Thomas and M. Ruben, *Dalton Trans.*, 2019, **48**, 15321–15337.
35 J. Olguin, *Coord. Chem. Rev.*, 2020, **407**, 213148.
36 Spin Crossover in Transition Metal Compounds I-III, in *Topics in Current Chemistry*, ed. P. Gütlich and H. A. Goodwin, Springer-Verlag, Berlin-Heidelberg-New York, 2004, vol. 233–235.
37 M. A. Halcrow, *Spin-Crossover Materials*, John Wiley & Sons, Ltd, Chichester, United Kingdom, 2013.
38 H. Phan, J. J. Hrudka, D. Igimbayeva, L. M. L. Daku and M. Shatruk, *J. Am. Chem. Soc.*, 2017, **139**, 6437–6447.
39 O. Kahn, *Molecular Magnetism*, VCH Publishers, Weinheim, 1993, pp. 59–69.
40 P. Guionneau, J.-F. Létard, D. S. Yufit, D. Chasseau, G. Bravic, A. E. Goeta, J. A. K. Howard and O. Kahn, *J. Mater. Chem.*, 1999, **9**, 985–994.
41 M. Mikolasek, G. Félix, W. Nicolazzi, G. Molnar, L. Salmon and A. Bousseksou, *New J. Chem.*, 2014, **38**, 1834–1839.
42 C. Enachescu, C. M. Nishino and S. Miyashita, in *Spin-Crossover Materials*, ed. M. A. Halcrow, Wiley, Chichester, 2013, vol. 18, pp. 455–474.
43 M. Sorai, *Bull. Chem. Soc. Jpn.*, 2001, **74**, 2223–2253.
44 B. Weber and F. A. Walker, *Inorg. Chem.*, 2007, **46**, 6794–6803.
45 M. P. Shores, C. M. Klug and S. R. Fiedler, in *Spin-Crossover Materials*, ed. M. A. Halcrow, Wiley, Chichester, 2013, vol. 10, pp. 281–302.
46 C. P. Slichter and H. G. Drickamer, *J. Chem. Phys.*, 1972, **56**, 2142–2160.
47 M. Sorai and S. Seki, *J. Phys. Chem. Solids*, 1974, **35**, 555–570.
48 A. Bousseksou, G. Molnar and G. Matouzenko, *Eur. J. Inorg. Chem.*, 2004, 4353–4369.
49 A. Bousseksou, G. Molnar, L. Salmon and W. Nicolazzi, *Chem. Soc. Rev.*, 2011, **40**, 3313–3335.
50 P. Gutlich, A. B. Gaspar and Y. Garcia, *Beilstein J. Org. Chem.*, 2013, **9**, 342–391.
51 G. Molnar, L. Salmon, W. Nicolazzi, F. Terki and A. Bousseksou, *J. Mater. Chem. C*, 2014, **2**, 1360–1366.
52 M. D. Manrique-Juarez, S. Rat, L. Salmon, G. Molnar, C. M. Quintero, L. Nicu, H. J. Shepherd and A. Bousseksou, *Coord. Chem. Rev.*, 2016, **308**, 395–408.
53 A. B. Gaspar and M. Seredyuk, *Coord. Chem. Rev.*, 2014, **268**, 41–58.
54 A. B. Gaspar, V. Ksenovontov, M. Seredyuk and P. Gütlich, *Coord. Chem. Rev.*, 2005, **249**, 2661–2676.
55 K. S. Kumar and M. Ruben, *Coord. Chem. Rev.*, 2017, **346**, 176–205.
56 Y. S. Meng and T. Liu, *Acc. Chem. Res.*, 2019, **52**, 1369–1379.
57 M. Darawsheh, L. A. Barrios, O. Roubeau, S. J. Teat and G. Aromi, *Angew. Chem., Int. Ed.*, 2018, **57**, 13509–13513.
58 A. Kawamura, J. Xie, J. N. Boyn, K. A. Jesse, A. J. McNeece, E. A. Hill, K. A. Collins, J. A. Valdez-Moreira, A. S. Filatov, J. W. Kurutz, D. A. Mazziotti and J. S. Anderson, *J. Am. Chem. Soc.*, 2020, **142**, 17670–17680.
59 H. J. Shepherd, C. M. Quintero, G. Molnar, L. Salmon and A. Bousseksou, in *Spin-Crossover Materials*, ed. M. A. Halcrow, Wiley, Chichester, 2013, vol. 13, pp. 347–373.
60 T. Lathion, A. Furstenberg, C. Besnard, A. Hauser, A. Bousseksou and C. Piguet, *Inorg. Chem.*, 2020, **59**, 1091–1103.
61 T. Lathion, L. Guénée, C. Besnard, A. Bousseksou and C. Piguet, *Chem. – Eur. J.*, 2018, **24**, 16873–16888.
62 C. Piguet, B. Bocquet and G. Hopfgartner, *Helv. Chim. Acta*, 1994, **77**, 931–942.
63 C. E. Hadden, *Magn. Reson. Chem.*, 2005, **43**, 330–333.
64 K. Nakamoto, *J. Phys. Chem.*, 1960, **64**, 1420–1425.
65 C. Piguet, J.-C. G. Bünzli, G. Bernardinelli, C. G. Bochet and P. Froidevaux, *J. Chem. Soc., Dalton Trans.*, 1995, 83–97.
66 S. Xu, J. E. T. Smith and J. M. Weber, *Inorg. Chem.*, 2016, **55**, 11937–11943.
67 E. R. Malinowski and D. G. Howery, *Factor Analysis in Chemistry*, Wiley, New York, Chichester, 1980.
68 H. Gampp, M. Maeder, C. J. Meyer and A. D. Zuberbuehler, *Talanta*, 1985, **32**, 1133–1139.
69 H. Gampp, M. Maeder, C. J. Meyer and A. D. Zuberbuehler, *Talanta*, 1986, **33**, 943–951.
70 B. R. Hall, L. E. Manck, I. S. Tidmarsh, A. Stephenson, B. F. Taylor, E. J. Blaikie, D. A. Vander Griend and M. D. Ward, *Dalton Trans.*, 2011, **40**, 12132–12145.
71 M. Maeder and P. King, Analysis of Chemical Processes, Determination of the Reaction Mechanism and Fitting of Equilibrium and Rate Constants, in *Chemometrics in Practical Applications*, ed. K. Varmuza, InTech., 2012, ISBN: 978-953-51-0438-4, DOI: 10.5772/31896.
72 *ReactLab™ Equilibria* (previously Specfit/32), Jplus Consulting Pty. Ltd., Palmyra WA 6957, Australia: http://jplusconsulting.com/products/reactlab-equilibria/.
73 L. Alderighi, P. Gans, A. Ienco, D. Peters, A. Sabatini and A. Vacca, *Coord. Chem. Rev.*, 1999, **184**, 311–318, http://www.hyperquad.co.uk/hyss.htm.
74 L. Aboshyan-Sorgho, T. Lathion, L. Guénée, C. Besnard and C. Piguet, *Inorg. Chem.*, 2014, **53**, 13093–13104.
75 R. M. Smith and A. E. Martell, *Critical Stability Constants*, Plenum, New York, 1982, vol. 5, pp. 235–253.
76 M. Borkovec, J. Hamacek and C. Piguet, *Dalton Trans.*, 2004, 4096–4105.
77 J. Hamacek, M. Borkovec and C. Piguet, *Dalton Trans.*, 2006, 1473–1490.
78 C. Piguet, *Chem. Commun.*, 2010, **46**, 6209–6231.
79 S. W. Benson, *J. Am. Chem. Soc.*, 1958, **80**, 5151–5154.
80 G. Ercolani, C. Piguet, M. Borkovec and J. Hamacek, *J. Phys. Chem. B*, 2007, **111**, 12195–12203.

81 G. Calzaferri, *Phys. Chem. Chem. Phys.*, 2017, **19**, 10611–10621.
82 H. Irving and R. J. P. Williams, *J. Chem. Soc.*, 1953, 3192–3210.
83 P. W. Dimmock, P. Warwick and R. A. Robbins, *Analyst*, 1995, **120**, 2159–2170.
84 B. J. Coe and S. J. Glenwright, *Coord. Chem. Rev.*, 2000, **203**, 5–80.
85 M. A. Robinson, D. H. Busch and J. D. Curry, *Inorg. Chem.*, 1963, **2**, 1178–1181.
86 A. B. P. Lever, *Inorganic Electronic Spectroscopy*, Elsevier, Amsterdam-Oxford-New York-Tokyo, 1984, p. 126.
87 S. M. Hart, J. C. A. Boeyens and R. D. Hancock, *Inorg. Chem.*, 1983, **22**, 982–986.
88 B. N. Figgis and M. A. Hitchman, *Ligand Field Theory and its Applications*, Wiley-VCH, New York, NY, USA, 2000.
89 B. Weber and F. A. Walker, *Inorg. Chem.*, 2007, **46**, 6794–6803.
90 A. A. Pavlov, G. L. Denisov, M. A. Kiskin, Y. V. Nelyubina and V. V. Novikov, *Inorg. Chem.*, 2017, **56**, 14759–14762.
91 D. F. Evans, *J. Chem. Soc.*, 1959, 2003–2005.
92 T. H. Crawford and J. Swanson, *J. Chem. Educ.*, 1971, **48**, 382–386.
93 J. Löliger and R. Scheffold, *J. Chem. Educ.*, 1972, **49**, 646–647.
94 D. Ostfeld and I. A. Cohen, *J. Chem. Educ.*, 1972, **49**, 829.
95 D. H. Grant, *J. Chem. Educ.*, 1995, **72**, 39–40.
96 C. Piguet, *J. Chem. Educ.*, 1997, **74**, 815–816.
97 H. Toftlund, *Coord. Chem. Rev.*, 1989, **94**, 67–108.
98 H. Toftlund, *Monatsh. Chem.*, 2001, **132**, 1269–1277.
99 S. Rodriguez-Jimenez, A. S. Barltrop, N. G. White, H. L. C. Feltham and S. Brooker, *Inorg. Chem.*, 2018, **57**, 6266–6282.
100 S. Singh and S. Brooker, *Inorg. Chem.*, 2020, **59**, 1265–1273.
101 C. Piguet, *Dalton Trans.*, 2011, **40**, 8059–8071.
102 D. M. Ford, *J. Am. Chem. Soc.*, 2005, **127**, 16167–16170.
103 E. B. Starikov, *J. Appl. Solution Chem. Model.*, 2013, **2**, 240–245.
104 O. A. Khakhel and T. P. Romashko, *J. Phys. Chem. A*, 2016, **120**, 2035–2040.
105 K. P. Kepp, *Inorg. Chem.*, 2016, **55**, 2717–2727.
106 P. W. Atkins and A. J. MacDermott, *J. Chem. Educ.*, 1982, **59**, 359–360.
107 G. Schreckenbach, *Chem. – Eur. J.*, 2017, **23**, 3797–3803.
108 L. Onsager, *J. Am. Chem. Soc.*, 1936, **58**, 1486–1492.
109 D. V. Matyushov, *J. Chem. Phys.*, 2004, **120**, 1375–1382.
110 C. J. Cramer and D. G. Truhlar, *Acc. Chem. Res.*, 2008, **41**, 760–768.
111 L. E. Johnson, S. J. Benight, R. Barnes and B. H. Robinson, *J. Phys. Chem. B*, 2015, **119**, 5240–5250.
112 L. Babel, T. N. Y. Hoang, L. Guénée, C. Besnard, T. A. Wesolowski, M. Humbert-Droz and C. Piguet, *Chem. – Eur. J.*, 2016, **22**, 8113–8123.
113 Y. Furusho, H. Goto, K. Itomi, H. Katagiri, T. Miyagawa and E. Yashima, *Chem. Commun.*, 2011, **47**, 9795–9797.
114 D. Furushou, T. Hashibe, T. Fujinami, K. Nishi, H. Hagiwara, N. Matsumoto, Y. Sunatsuki, M. Kojima and S. Iijima, *Polyhedron*, 2013, **52**, 1489–1498.
115 SHAPE is a free software developed by M. Llunell, D. Casanova, J. Cirera, P. Alemany and S. Alvarez, and available online at http://www.ee.ub.edu/.
116 A. G. Orpen, L. Brammer, F. H. Allen, O. Kennard, D. G. Watson and R. Taylor, *J. Chem. Soc., Dalton Trans.*, 1989, S1–S83.
117 F. H. Allen, O. Kennard, D. G. Watson, L. Brammer, A. G. Orpen and R. Taylor, *J. Chem. Soc., Perkin Trans. 2*, 1987, S1–S19.
118 N. Sasaki and T. Kambara, *Phys. Rev. B: Condens. Matter Mater. Phys.*, 1989, **40**, 2442–2449.
119 B. J. C. Vieira, J. T. Coutinho, I. C. Santos, L. C. J. Pereira, J. C. Waerenborgh and V. da Gama, *Inorg. Chem.*, 2013, **52**, 3845–3850.
120 D. Chernyshov, M. Hostettler, K. W. Tornroos and H. B. Burgi, *Angew. Chem., Int. Ed.*, 2003, **42**, 3825–3830.
121 P. Lian, H. Wei, C. Zheng, Y. Nie, J. Bian, Z. Bian and C. Huang, *Dalton Trans.*, 2011, **40**, 5476–5482.
122 W. C. Wolsey, *J. Chem. Educ.*, 1973, **50**, A335–A337.
123 J.-L. Pascal and F. Favier, *Coord. Chem. Rev.*, 1998, **178–180**, 865–902.
124 G. A. Bain and J. F. Berry, *J. Chem. Educ.*, 2008, **85**, 532.
125 G. M. Sheldrick, *Acta Crystallogr., Sect. A: Found. Crystallogr.*, 2008, **64**, 112–122.
126 M. C. Burla, M. Camalli, B. Carrozzini, G. L. Cascarano, C. Giacovazzo, G. Polidori and R. Spagna, *Acta Crystallogr., Sect. A: Found. Crystallogr.*, 1999, **55**, 991–999.
127 G. M. Sheldrick, *Acta Crystallogr., Sect. C: Struct. Chem.*, 2015, **71**, 3–8.